



Peer review status:

This is a non-peer-reviewed preprint submitted to EarthArXiv.

1 Q_{M1D} : A 1D model of shear attenuation in the mantle from
2 differential body waves

3 Carl Martin^{1,2*}, Sujania Talavera-Soza¹ & Arwen Deuss¹

4 ¹ Department of Geosciences, Utrecht University, 3584 CB, Netherlands

5 ² Research School of Earth Sciences, The Australian National University, Canberra, ACT
6 0200, Australia

7 *Corresponding author (carl.martin@anu.edu.au)

8 **Abstract**

9 We introduce a new 1D model of shear attenuation in the mantle (Q_{M1D}) constructed from mea-
10 surements of differential attenuation of S and ScS body waves. We build a dataset of over 90,000
11 measurements of $\delta t_{\text{ScS-S}}^*$ from seismograms with high-quality S and ScS waveforms from deep earth-
12 quakes between 20–75° epicentral distance from 1990–2024. To ensure that measurements are
13 robust, we require that values of differential attenuation are similar between the instantaneous
14 frequency matching and waveform matching methods. Using this dataset, we perform a Bayesian
15 inversion to construct 1D profiles of mantle shear attenuation Q_{μ} and its uncertainties. Our dataset
16 has a high sensitivity to the mid-mantle (750–2200 km) corresponding to the turning depths of the
17 S phases, which maps into lower uncertainty in the ensemble distribution at these depths. Q_{M1D}
18 suggests that the mantle is more attenuating than PREM on average; but, notably, that there is
19 a high attenuating layer around 750 km depth and that there are low attenuating layers around
20 900 km and 2000 km depth. Due to the source-receiver distribution for the phases, our dataset
21 has a sampling bias in the mantle around the edge of the Pacific. These weakly attenuating zones
22 in the mantle may correspond to a viscosity jump around 900 km depth and a further viscosity
23 jump in the deep mantle around 2000 km depth, whilst the thin strongly attenuating layer may

24 correspond to regions of slab stagnation caused by a potential thin layer of low viscosity beneath
25 the mantle transition zone.

26 **1 Introduction**

27 Over the past decades, elastic tomography models of the mantle have been numerous and are
28 becoming increasingly detailed [e.g. Dziewonski and Anderson, 1984; Ritsema et al., 2011; Cui
29 et al., 2024]. However, it is equally important to understand the anelastic structure since it results
30 in variations in the amplitude of seismic phases [e.g. Romanowicz, 1995; Dalton and Ekström, 2006;
31 Zaroli et al., 2010; Hansen et al., 2021] – which may otherwise be mapped into elastic structure [e.g.
32 Karato, 1993; Chaves and Ritsema, 2016] – but also because the anelastic structure is thought to be
33 much more sensitive to temperature and grain size variations in the mantle than elastic structure is
34 [e.g. Jackson et al., 1992, 2002; Matas and Bukowinski, 2007; Faul and Jackson, 2015]. Knowledge
35 of both elastic and anelastic structure will therefore result in important additional constraints on
36 mantle dynamics, but also in distinguishing between the chemical and thermal composition of the
37 mantle [e.g. Romanowicz, 1995; Cooper, 2002; Gung and Romanowicz, 2004].

38 Whilst the large-scale anelastic structure of upper mantle, i.e. attenuation, is relatively well
39 understood from body and surface waves [e.g. Romanowicz, 1995; Bhattacharyya et al., 1996; Reid
40 et al., 2001; Romanowicz and Gung, 2002; Gung and Romanowicz, 2004; Dalton et al., 2008; Adenis
41 et al., 2017; Karaoğlu and Romanowicz, 2018] – where an anti-correlation is found between 3D per-
42 turbations in velocity and attenuation – there have been significantly fewer studies on attenuation
43 in the lower mantle. The large-scale attenuation structure of the lower mantle is predominantly
44 constrained by normal mode observations [e.g. Dziewonski and Anderson, 1984; Moulik and Ek-
45 ström, 2025] and is typically assumed to be less attenuating than the upper mantle [e.g. Warren
46 and Shearer, 2002; Souriau et al., 2012; Nguyen et al., 2025]. There have been attempts to distin-
47 guish relative attenuation within and outside the two antipodal Large Low Shear Velocity Provinces
48 (LLSVPs) using body waves [Romanowicz, 1995; Hwang and Ritsema, 2011; Liu and Grand, 2018]
49 to provide much needed constraints on the grain size, temperature, and longevity of these struc-
50 tures. A recent study by Talavera-Soza et al. [2025] used anelastic normal mode splitting function
51 observations to construct a 3D model of attenuation of the mantle. Their model, QS4L3, is in

52 good agreement with attenuation observations from body waves and surface waves in the upper
53 mantle, but appears to differ from the few studies of the lowermost mantle which use body waves.
54 In particular, normal modes find LLSVPs to be weakly attenuating – suggesting large grain sizes
55 and high temperatures, which potentially implies a long-lived structure [Talavera-Soza et al., 2025]
56 – whilst body waves studies have suggested the opposite [Romanowicz, 1998; Lawrence and Wysession,
57 2006; Hwang and Ritsema, 2011; Liu and Grand, 2018]. It is important to note that the
58 datasets used in each of the studies of the lower mantle are typically small and that the frequency
59 content differs by a few orders of magnitude between body waves and normal modes. Given there
60 is significant variability and scatter in measurements of attenuation [e.g. Bhattacharyya, 1998], the
61 nature of anelasticity in the lowermost mantle remains unclear. In this study, we therefore aim to
62 elucidate the anelastic structure of the lower mantle.

63 Attenuation t^* (with units of seconds) of a body wave phase is defined as the shear quality
64 factor Q_μ (dimensionless) integrated along the raypath

$$t^* = \int \frac{ds}{\beta Q_\mu} = \int_s \frac{dt}{Q_\mu} \quad (1)$$

65 where s defines the raypath and β is the shear velocity. This is also sometimes related to the path
66 averaged quality factor Q_{phase} as $t^* = T_{\text{phase}}/Q_{\text{phase}}$ for the total travel time T_{phase} of a given body
67 wave phase. It is not possible to directly measure t^* , but it is possible to measure the relative
68 attenuation between a target phase with t_{TARG}^* and a reference phase with t_{REF}^* as

$$\delta t_{\text{REF-TARG}}^* = t_{\text{REF}}^* - t_{\text{TARG}}^* = \int_{\text{REF}} \frac{dt}{Q_\mu} - \int_{\text{TARG}} \frac{dt}{Q_\mu} \quad (2)$$

69 There have been many methods used over the past decades to make measurements of relative
70 attenuation of body waves. These can be categorised as frequency domain or time domain methods,
71 but the principle of both methods is the same: when a signal is attenuated, the higher frequency
72 content is more attenuated than the lower frequency content resulting in a broadened signal [e.g.
73 Teng, 1968; Quan and Harris, 1997]. In the frequency domain, the spectral ratio method is by far
74 the most commonly used method [e.g. Sheehan and Solomon, 1992; Bhattacharyya et al., 1996; Roth
75 et al., 1999; Fisher et al., 2003; Lawrence and Wysession, 2006; Hwang and Ritsema, 2011; Suetsugu

76 et al., 2019; Soto Castaneda et al., 2021; Nguyen et al., 2025], which relates the spectral amplitude
77 ratio to the relative attenuation between two signals. A more sophisticated frequency domain
78 method – the instantaneous frequency matching method (IFM) – applies the causal attenuation
79 operator to the target signal until its instantaneous frequency matches that of the reference signal
80 [e.g. Matheney and Nowack, 1995; Quan and Harris, 1997; Ford et al., 2012; Durand et al., 2013; Sun
81 et al., 2025]. In the time domain, the waveform matching (WM) method finds the optimal relative
82 attenuation that matches the waveforms between the target signal which has been attenuated by
83 the causal attenuation operator and the reference signal [e.g. Chan and Der, 1988; Bhattacharyya,
84 1998; Reid et al., 2001; Oki and Shearer, 2008; Bezada et al., 2023]. This is also sometimes done
85 in a joint inversion for the amplitude ratio, time delay and source parameters [e.g. Reid et al.,
86 2001; Garcia et al., 2013; Pejić et al., 2017]. Additionally, implicit inversion of Q_μ structure has
87 also been performed by waveform modelling of amplitude ratios [e.g. Revenaugh and Jordan, 1991;
88 Chaves and Ritsema, 2016; Konishi et al., 2017, 2020; Borgeaud and Deschamps, 2021], but this
89 has significant trade-offs with elastic structure. Each of these methods has its own advantages and
90 disadvantages – and no one method works in every situation [e.g. Bhattacharyya, 1998; Ford et al.,
91 2012] – so the most appropriate method(s) to use depends on the context of the investigation.
92 It is important to note that all of the methods described above result in inaccurate estimates of
93 attenuation when there are interfering phases in the target or reference seismic waveforms.

94 The choice of which reference and target signals to use can also be broadly categorised into
95 three different types:

- 96 1. The first is to estimate the relative attenuation of the target and reference signals for two
97 different seismic phases recorded on the same station for the same event; e.g. ScSScS-ScS
98 [Revenaugh and Jordan, 1991], sS-S and sScS-ScS [Flanagan and Wiens, 1994], and ScS-S
99 [Durand et al., 2013]. Any differential attenuation is then attributed to the difference between
100 the two raypaths travelled by the two phases, since the source and receiver contributions to
101 attenuation are assumed to be similar for both raypaths.
- 102 2. The second is to estimate the attenuation of the same seismic phase for the same event
103 recorded on different stations [e.g. Warren and Shearer, 2002; Hwang et al., 2009]. In this
104 case, the ‘source term’ – a contribution to the measurement from source effects – is assumed

105 to be negligible since the raypaths travelled by a phase are similar near the source. However,
106 the ‘station term’ – the contribution to the measurement due to near-station effects – must
107 be accounted for. One important consideration in using this method is that rupture direc-
108 tivity modifies the source frequency spectra as a function of the take-off angle [e.g. Bernard
109 et al., 1996], so any inferred attenuation difference between pairwise stations includes both
110 differential attenuation structure and source frequency spectra variations [e.g. Warren and
111 Shearer, 2006]. To overcome this, station pairs can be chosen so that they are azimuthally
112 similar [e.g. Hwang and Ritsema, 2011].

- 113 3. The third is to estimate the ‘absolute’ attenuation of an observed phase relative to synthetic
114 waveforms, in which case both source and station effects must be accounted for in the synthetic
115 modelling in order to get accurate results [e.g. Zhu et al., 2022; Sun et al., 2025]. Equivalently,
116 by assuming a source model and the station response [e.g. Brune, 1970; Scherbaum, 1990], it
117 is possible to estimate the ‘absolute’ attenuation of a signal by directly fitting its frequency
118 spectra [e.g. Rietbrock, 2001; Eberhart-Phillips and Chadwick, 2002].

119 Source and station terms can be inverted for – as well as Q_μ , but at additional computational
120 expense – assuming that these terms are consistent for a given source or station, and that individual
121 sources and stations are represented in the dataset multiple times [e.g. Roth et al., 1999; Warren
122 and Shearer, 2002; Hwang et al., 2009]. Historically, ScS reverberations have been used to make
123 whole-mantle estimates of average Q_{ScS} in corridors between pairs of sources and receivers [e.g.
124 Chan and Der, 1988; Revenaugh and Jordan, 1991; Isse and Nakanishi, 1997; Gomer and Okal,
125 2003; Kanamori and Rivera, 2015; Chaves and Ritsema, 2016], which minimises the effect of source
126 and station terms. However, this choice of phases involves unpaired raypaths travelling through
127 the upper mantle and crust, so accurate upper mantle and crustal models are required to correct
128 for these effects or the results could be significantly biased [e.g. Revenaugh and Jordan, 1991; Isse
129 and Nakanishi, 1997]. Additionally, S reflections off the underside of Earth’s surface have highly
130 complex mini-max Fresnel zones and so poorly match ray theoretical approximations [e.g. Shearer,
131 1993; Schultz and Gu, 2013]. It is thus difficult to make corrections for unpaired raypaths through
132 the crust. This is also the case when comparing synthetics to data to estimate attenuation [e.g.
133 Sun et al., 2025].

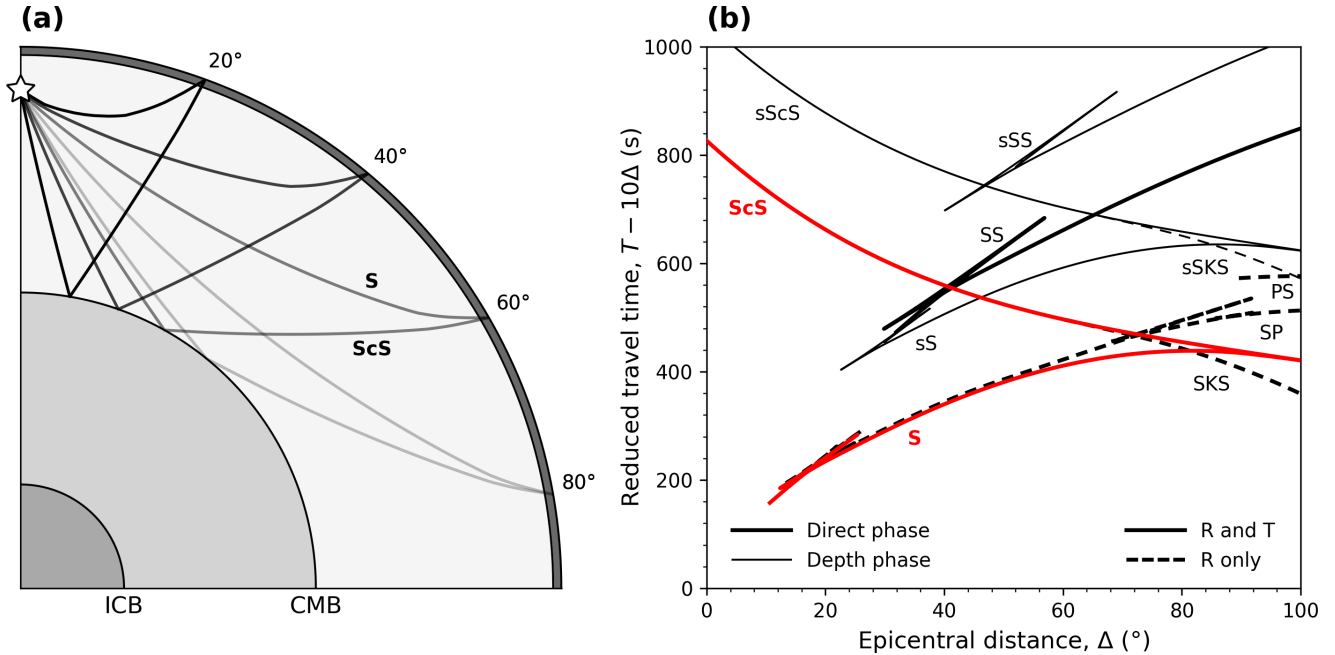


Figure 1: **(a)** S and ScS raypaths for a range of epicentral distances. The turning depths of S and differential incident and take-off angles of S and ScS are shown in Figure S1. **(b)** The reduced travel times of seismic phases observed around S and ScS (highlighted in red). The visibility of phases on the transverse (T) and radial (R) components for an isotropic model is indicated as R and T (solid line) or R only (dashed line).

134 Ford et al. [2012] and Durand et al. [2013] used S and ScS – which minimises the effects of
 135 source and station terms, and has no unpaired raypaths travelling through the crust – to estimate
 136 the shear attenuation profile of the mantle. S turns in the mid-mantle, whilst ScS is reflected off the
 137 core-mantle boundary (CMB, Figure 1a). At long epicentral distances, the raypaths of S and ScS,
 138 and the difference in take-off and incident angles between S and ScS, are very similar (Figures 1a &
 139 S1), but the travel time differential becomes too small to distinguish between them on seismograms
 140 (Figure 1b). At short epicentral distances, the difference in take-off and incident angles becomes
 141 large, and so the assumption that the near-source terms cancel out becomes strained [e.g. Ford et al.,
 142 2012]. However, some have suggested that this effect is negligible for frequency domain methods,
 143 even for phases with opposite take-off angles [e.g. Flanagan and Wiens, 1994]. The differential
 144 attenuation of ScS and S is sensitive to the whole depth range of the mantle, but significantly
 145 less sensitive in the uppermost mantle and crust where the raypaths are most similar. Assuming
 146 a radially isotropic Earth, the relative attenuation of ScS and S would therefore predominantly
 147 depend on the turning depth of the S raypath (Figures 1a & S1a-b).

148 In this study, we compile a dataset of over 90,000 high-quality S and ScS waveforms and
149 estimate their relative attenuation $\delta t_{\text{ScS-S}}^*$ to make inferences about 1D mantle shear attenuation.
150 We evaluate three commonly used methods to estimate differential attenuation (spectral ratio,
151 instantaneous frequency matching, and waveform matching). After weighing the advantages and
152 disadvantages of each of the methods, we disregard the spectral ratio method, and analyse and
153 compare our dataset of S and ScS waveforms with the instantaneous frequency matching (IFM)
154 and waveform matching (WM) methods. Finally, we perform a Bayesian inversion to fit a 1D
155 whole-mantle model of Q_μ to our dataset, which also includes estimates of uncertainty in the
156 profile.

157 2 Methods

158 2.1 Data

159 We inspected seismograms of earthquakes larger than magnitude 6.0 and deeper than 75 km depth
160 between 1990–2024 from the EarthScope SAGE event catalogue. We only downloaded seismograms
161 for stations between epicentral distances 20–80°, since S is not distinguishable from surface waves
162 at shorter distances and ScS at longer distances. We ensure that S phases at short epicentral
163 distances do not appear to be contaminated by triplication, which may result in phase broadening
164 (discussed in Section 4.1). 75 km is chosen as the event depth threshold since the arrival time
165 difference between S and ScS and their respective depth phases (sS and sScS) is approximately
166 twice the dominant period of S (~ 14 s). The instrument response is removed and the traces output
167 as velocity, before being downsampled to 10 Hz and rotated to the ZRT orientation.

168 To avoid issues of seismic phase interference in our measurements, we disregard seismograms
169 for which the arrival time of ScS is within 25 s of S, sS, SS or SSS as calculated for the Preliminary
170 Reference Earth Model (PREM) [Dziewonski and Anderson, 1984]. We then compute the signal-
171 to-noise (SNR) of the seismic phases, defined as the ratio between the maximum amplitude in a
172 window of ± 15 s around the predicted S or ScS arrival and the root mean square of the window
173 120–20 s before the predicted S arrival. We then discard any seismograms for which the SNR of
174 S or ScS are less than 5, or if the maximum amplitude is at the edge of the 30 s window around
175 either phase.

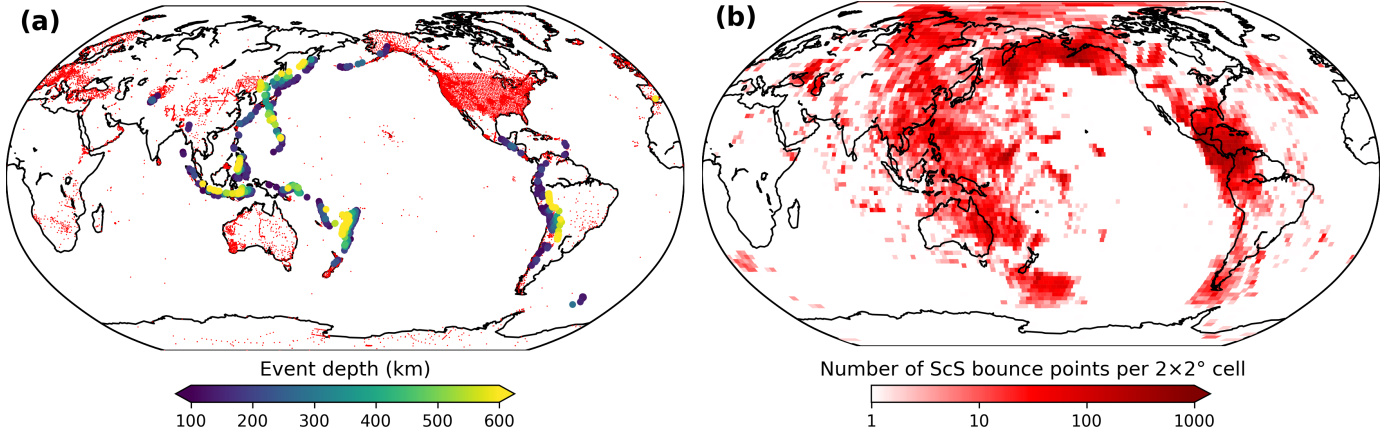


Figure 2: **(a)** Locations of earthquakes (circles, coloured by event depth) and stations (red dots) used in this study. **(b)** Number of ScS bounce points per $2 \times 2^\circ$ quasi-equal area cell.

176 The sources and receivers represented in our final dataset are shown in Figure 2a. For a quasi-
 177 equal area grid of the core-mantle boundary (CMB), we plot the number of ScS bounce points per
 178 $2 \times 2^\circ$ cell in Figure 2b, which shows that coverage of the mantle of our dataset is strongly biased
 179 by the source-receiver distribution around the edge of the Pacific.

180 2.2 Estimating differential attenuation of body waves

181 2.2.1 Spectral ratio method

182 The spectral ratio method of estimating relative attenuation has been known for over 60 years
 183 [e.g. Asada and Takano, 1963; Kovach and Anderson, 1964], in which the gradient of the spectral
 184 ratio between two signals can be related to the relative attenuation between the signals assuming
 185 frequency independence of Q . This method suffers from significant technical challenges pertaining
 186 to the windowing and tapering of signals, spectral gaps, and the choice of frequency range over
 187 which to estimate the gradient of the spectral ratio [e.g. Bhattacharyya, 1998; Ford et al., 2012;
 188 Tanaka and Tkalčić, 2015]. Whilst these shortfalls have been resolved to some extent – e.g. using
 189 multi-tapering of seismic phases to reduce spectral leakage [Thomson, 1982; Lees and Park, 1995]
 190 – we find that the calculated δt^* values depend strongly on the setup parameters and SNR of the
 191 data. Notably, there was often very low similarity between the spectral ratio and its best linear fit,
 192 as previously observed by Isse and Nakanishi [1997]. To improve the quality of fit, some studies have
 193 also stacked data within a vertical column from ScS multiples and surface reflections to increase the

194 SNR of the waveforms [e.g. Gomer and Okal, 2003; Suetsugu et al., 2019], though this assumption
 195 is only reasonable for short epicentral distances and not practical for a broader global study. Others
 196 have performed joint fitting of spectral phase and amplitude ratios [e.g. Eilon and Abers, 2017].

197 **2.2.2 Instantaneous frequency matching method**

198 As attenuation preferentially diminishes higher frequency spectra, the average and peak frequencies
 199 will appear lower for more attenuated waves [e.g. Matheney and Nowack, 1995; Quan and Harris,
 200 1997]. Matheney and Nowack [1995] derived that the differential attenuation between two signals
 201 is equivalent to the value t_{CAO}^* of the causal attenuation operator that matches the instantaneous
 202 frequency of the target signal f_{TARG}^* to that of the reference signal f_{REF} (Figure 3a-e). The causal
 203 attenuation operator $D(\omega)$ takes the form

$$D(\omega) = \exp \left[\frac{-\omega t_{\text{CAO}}^*}{2} \left(1 - \frac{2i}{\pi} \ln \frac{\omega}{\omega_0} \right) \right] \quad (3)$$

204 where t_{CAO}^* is the relative attenuation factor between two phases, ω is angular frequency, and ω_0
 205 is a reference angular frequency (usually taken to be 1 Hz) [e.g. Chapman et al., 1988; Aki and
 206 Richards, 2002]. Since $t_{\text{CAO}}^* \geq 0$ s, whichever signal has the lowest instantaneous frequency is taken
 207 as the reference and the other as the target signal (Figure 3c-e).

208 The instantaneous amplitude (envelope) $a(t)$ and instantaneous phase $\phi(t)$ of a signal $y(t)$
 209 represented as a complex function are given as

$$y(t) = a(t) \exp [i\phi(t)], \quad a(t) = \sqrt{y(t)^2 + y^*(t)^2}, \quad \phi(t) = \tan^{-1} \left[\frac{y^*(t)}{y(t)} \right] \quad (4)$$

210 where $y^*(t)$ is the Hilbert transform of a signal $y(t)$, so the instantaneous frequency f_I is given by

$$f_I(t) = \frac{1}{2\pi} \frac{d\phi(t)}{dt} = \frac{1}{2\pi} \frac{y(t) \frac{dy^*(t)}{dt} - y^*(t) \frac{dy(t)}{dt}}{a^2(t) + \epsilon^2} \quad (5)$$

211 where ϵ is a small damping factor added to ensure numerical stability [e.g. Matheney and Nowack,
 212 1995].

213 It can be shown that the instantaneous centre frequency of the signal f_C is related to the

214 instantaneous frequency,

$$f_C = \frac{\int_0^\infty f A(f) df}{\int_0^\infty A(f) df} \equiv \frac{\int_0^\infty f_1(t) a(t)^2 dt}{\int_0^\infty a(t)^2 dt} \quad (6)$$

215 where $A(f)$ is the Fourier power spectrum [e.g. Barnes, 1993; Dasios et al., 2001], so the time-
216 averaged instantaneous centre frequency $f_C(t)$ is

$$f_C(t) \approx \frac{\int_{t-W}^{t+W} f_1(t') a(t')^2 dt'}{\int_{t-W}^{t+W} a(t')^2 dt'} \quad (7)$$

217 for a window of length $2W$ [Matheney and Nowack, 1995].

218 We perform an iterative search across t_{CAO}^* values with $W = 5$ s, beginning from 0–10 s in
219 increments of 1 s and decreasing by factors of 10 until we reach a precision of 10^{-2} s. For S and
220 ScS, if $f_S < f_{\text{ScS}}$ (i.e. S is more attenuated than ScS) then S is the reference phase and ScS is the
221 target phase, so $\delta t_{\text{ScS-S}}^* = -t_{\text{CAO}}^*$; otherwise $\delta t_{\text{ScS-S}}^* = t_{\text{CAO}}^*$ [e.g. Ford et al., 2012; Durand et al.,
222 2013].

223 2.2.3 Waveform matching method

224 Time domain methods have also been used to estimate relative attenuation of seismic phases [e.g.
225 Bhattacharyya, 1998; Reid et al., 2001]. The amplitude spectrum of S and ScS can be written as

$$A_S(\omega, \Delta) = S(\omega) R(\omega) I(\omega) G_S(\Delta) D(\omega, t_S^*) \exp[-i\omega t_S] \quad (8)$$

$$A_{\text{ScS}}(\omega, \Delta) = S(\omega) R(\omega) I(\omega) G_{\text{ScS}}(\Delta) D(\omega, t_{\text{ScS}}^*) \exp[-i\omega t_{\text{ScS}}] \quad (9)$$

226 where ω is the angular frequency, Δ is the epicentral distance, $S(\omega)$ is the source spectrum, $R(\omega)$
227 is the site response, $I(\omega)$ is the instrument response, $G(\omega, \Delta)$ includes the source radiation pattern
228 and geometric spreading, $D(\omega)$ is the causal attenuation operator as defined in Equation 3, and t_S
229 and t_{ScS} are the travel times of S and ScS, respectively [e.g. Reid et al., 2001]. Assuming that the
230 source spectrum, site response and instrument response are similar for both phases, we can relate
231 the spectra of S and ScS as

$$A_{\text{ScS}}(\omega, \Delta) = G_{\text{ScS-S}}(\Delta) A_S(\omega, \Delta) D(\omega, \delta t_{\text{ScS-S}}^*) \exp[-i\omega \delta t_{\text{ScS-S}}] \quad (10)$$

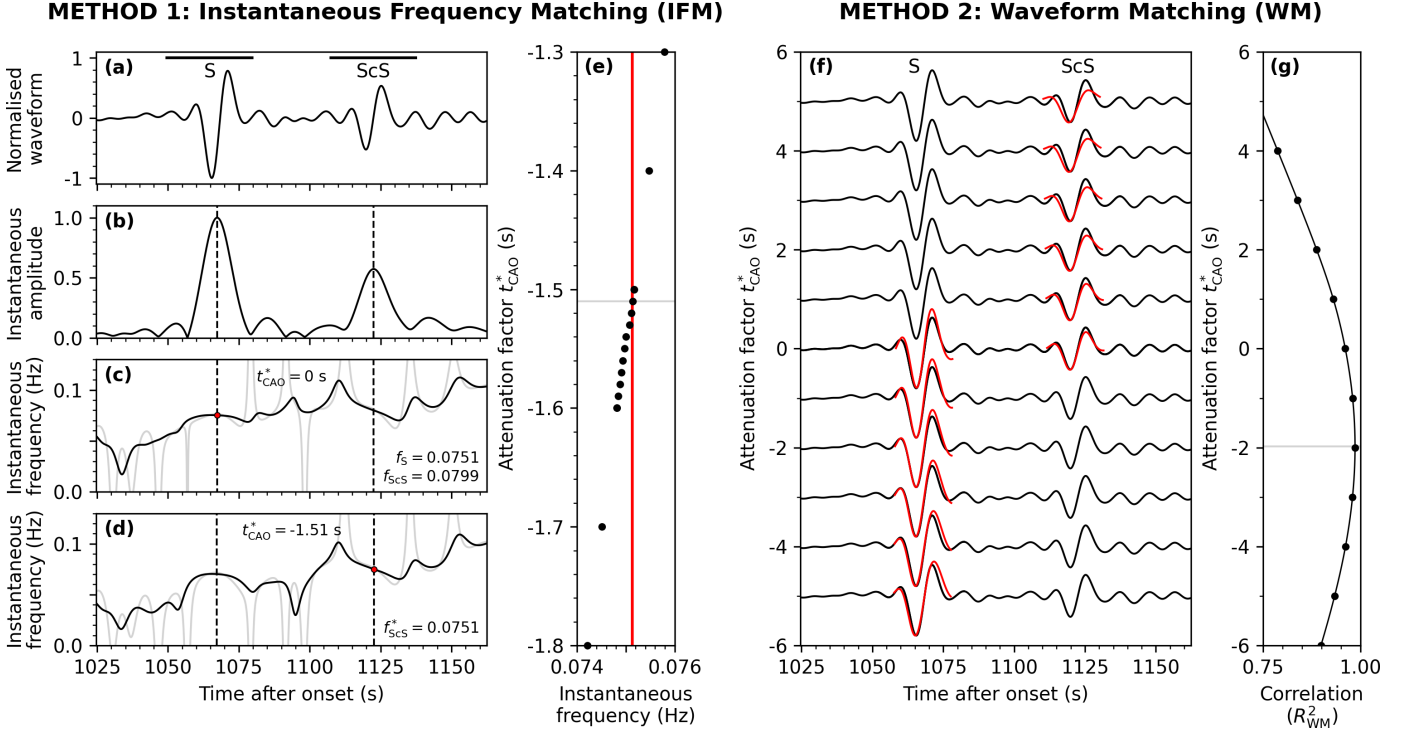


Figure 3: An overview of the two methods used to estimate differential attenuation between S and ScS in this study. Method 1 (**left**) is instantaneous frequency matching (IFM): **(a)** The transverse velocity seismogram for a Mw 6.6 earthquake occurring on 1997/11/28 in South America at 600 km depth, recorded at Southern California Seismic Network station PLM, bandpass filtered between 0.02–0.12 Hz. The black horizontal bar marks a window of ± 15 s around the predicted S and ScS arrival times from PREM. The corresponding **(b)** instantaneous amplitude and **(c)** instantaneous frequency of the trace. The dashed lines mark the peaks of instantaneous amplitudes which are used as the reference points to estimate the instantaneous frequencies of S and ScS. The black line is the instantaneous frequency which has been weighted by the instantaneous amplitude, whereas the light grey line is the unweighted instantaneous frequency of the waveform. **(d)** The instantaneous frequency of the trace which has been convolved with the attenuation operator with $t_{\text{CAO}}^* = -1.51$ s. The negative value indicates that S is more attenuated than ScS in this trace. **(e)** A range of values of t_{CAO}^* are trialled iteratively until the instantaneous frequency of the attenuated phase, f_{ScS}^* (black circles), matches the instantaneous frequency of the unattenuated reference phase, f_{S} (red line). Method 2 (**right**) is waveform matching (WM): **(f)** Waveforms which have been synthetically attenuated with different attenuation operator values (red) are overlaid on the original waveforms (black). For positive values of t_{CAO}^* , S waveforms have been attenuated and overlaid on the original ScS waveforms; for negative values of t_{CAO}^* , ScS waveforms have been attenuated and overlaid on the original S waveforms. **(g)** The correlation R_{WM}^2 between the attenuated and reference signals is calculated for a range of attenuation operator t_{CAO}^* values. The optimum relative attenuation between the two phases can then be estimated from interpolating between these values. The values of $\delta t_{\text{ScS-S}}^*$ for this event-station pair from IFM and WM are -1.51 s and -1.98 s, respectively.

232 where $G_{\text{ScS-S}}(\Delta) = G_{\text{ScS}}(\Delta)/G_{\text{S}}(\Delta)$ is a constant for a given event-station pair, $\delta t_{\text{ScS-S}}^* = t_{\text{ScS}}^* - t_{\text{S}}^*$
 233 and $\delta t_{\text{ScS-S}} = t_{\text{ScS}} - t_{\text{S}}$. For S and ScS, the assumption that the source spectra of both signals is
 234 the same is reasonable, as long as the take-off angles of the two phases are in the same lobe of the
 235 radiation pattern [e.g. Flanagan and Wiens, 1994].

236 In the time domain, the relative attenuation operator can therefore be found simply by min-
 237 imising the misfit between the reference and attenuated target waveforms (Figure 3f-g), which we
 238 quantify using the Pearson correlation coefficient R_{WM} . We apply the attenuation operator to the
 239 target waveforms for values of t_{CAO}^* between 0–10 in increments of 1 s for both S and ScS as the
 240 target signal (since either phase can be more attenuated), and calculate the associated correlation
 241 coefficient allowing the attenuated target waveform to shift in time to maximise similarity with the
 242 reference waveform. From this, we then interpolate between the observed correlation coefficients
 243 to identify the value of $\delta t_{\text{ScS-S}}^*$ as t_{CAO}^* with the maximum value of R_{WM} (Figure 3g). Some studies
 244 instead jointly determine the relative attenuation, amplitude ratio, time delay and source param-
 245 eters in a non-linear parameter inversion [e.g. Reid et al., 2001; Garcia et al., 2013; Pejić et al.,
 246 2017], but this additional complexity introduces trade-offs which are unnecessary unless the source
 247 terms for both phases are not similar.

248 Assuming that the geometric spreading factor, source radiation pattern, and reflection and
 249 transmission coefficients are well known, it is also possible to use a simplified approach to this
 250 method of directly inferring δt^* from the envelope ratios of two signals bandpass filtered in a narrow
 251 window. For example, this is a commonly used approach to image attenuation in the uppermost
 252 inner core from envelope ratios of PKiKP and PKIKP [e.g. Cao and Romanowicz, 2004; Waszek
 253 and Deuss, 2013], but has also been used in mantle imaging by comparing envelope amplitudes of S
 254 multiples with synthetic waveforms [Zhu et al., 2022] and comparing the amplitude ratios of s to ScS
 255 [Zhang et al., 2019]. Hansen et al. [2021] used a similar method to correct for relative attenuation
 256 effects between P and PcP waveforms to detect ultra-low velocity zones in the Antarctic region,
 257 but did not investigate spatial distributions or patterns of $\delta t_{\text{PcP-P}}^*$ values. Some studies using the
 258 spectral ratio method have also used an implicit form of this method to simply verify that the
 259 attenuated waveforms (using the attenuation factor determined by spectral division as t_{CAO}^* in the
 260 causal attenuation operator) matched the reference phase better than the unattenuated waveform,
 261 and discarded data for which a worse match was recovered, except for weakly attenuating data for

262 which this requirement was waived [e.g. Fisher et al., 2003; Lawrence and Wysession, 2006].

263 Waveform matching is less precise than frequency domain methods – which can be seen from the
264 wide range of t_{CAO}^* values that fit the waveforms almost equally well in Figure 3g compared to the
265 apparent high precision of the instantaneous frequency matching method in Figure 3e. However,
266 waveform matching does not suffer from the same issues as frequency domain methods with regards
267 to spectral holes – ‘missing’ amplitude in the spectral content – since it is taken as an average
268 measurement over a filter band [e.g. Tanaka and Tkalčić, 2015]. Bhattacharyya [1998] warns that
269 this time domain method can be contaminated by interfering phases resulting in a measurement
270 error of up to 2 s, and that they found frequency domain methods to be more accurate in synthetic
271 tests, but we address this by disregarding waveforms for which phase pairs are predicted to be too
272 close to distinguish (as discussed in Section 2.1).

273 **2.2.4 Combined fitting**

274 We thus opt for a joint fitting approach with the instantaneous frequency matching (IFM) and
275 waveform matching (WM) methods, as likewise recommended by studies that compared frequency
276 and time domain methods [e.g. Der and Lees, 1985; Dasios et al., 2001]. Agreement between the two
277 methods, which have different drawbacks and strengths, significantly increases confidence in the
278 values we obtain. Figure 4a shows the measurements of differential attenuation for IFM and WM,
279 where the points are coloured by the similarity R_{IFM}^2 between the reference and attenuated target
280 waveforms from the IFM method. (We note that, by definition of the methodology, $R_{\text{WM}}^2 \geq R_{\text{IFM}}^2$).
281 There are a number of results clustered around $\delta t_{\text{IFM}}^* = 0$ s, due to the way that S and ScS are
282 trialled as the target and reference phases, but these mainly occur for waveforms with low similarity
283 (Figure 4b). If we apply additional criteria to our dataset for a minimum similarity R_{C}^2 between
284 the reference and attenuated target waveforms, we find exceptionally good correlation Pearson
285 correlation $R > 0.9$ between the two methods (Figure 4b-c). Based on this analysis, we set a
286 further criteria that $R_{\text{IFM}}^2 \geq R_{\text{C}}^2 = 0.9$, and we require that the difference between the two methods
287 $\Delta t^* = |\delta t_{\text{WM}}^* - \delta t_{\text{IFM}}^*|$ is less than 3 s (Figure 4c). The measurement of differential attenuation is
288 then taken as the average of the two methods.

289 Following Ford et al. [2012], we apply a bandpass filter between 0.02–0.12 Hz on the waveforms
290 before estimating attenuation. We then also require that measurements of the weighted instan-

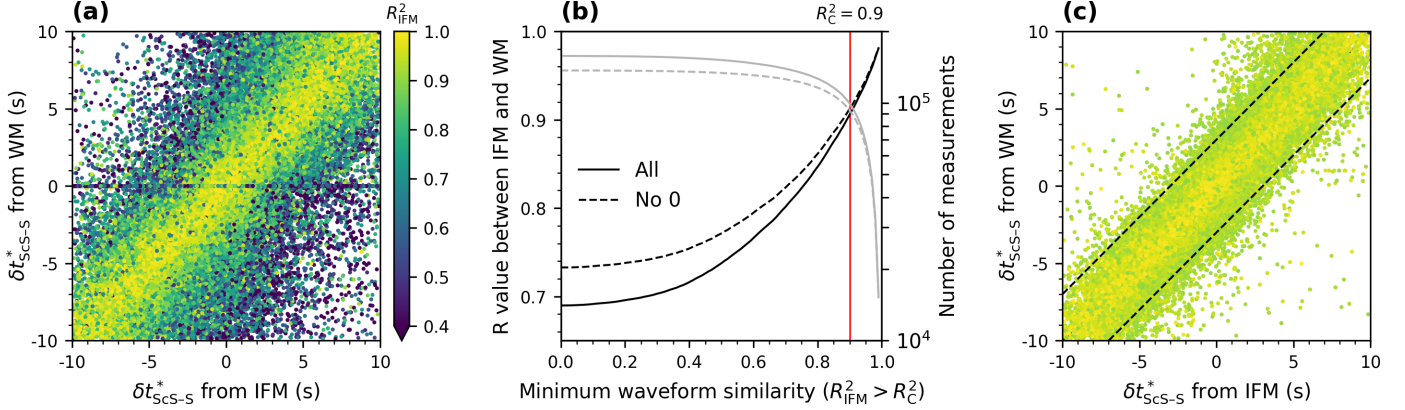


Figure 4: **(a)** A comparison of $\delta t_{\text{ScS-S}}^*$ measurements from the instantaneous frequency matching (IFM) and waveform matching (WM) methods. The colour of the data point corresponds to the correlation R_{IFM}^2 between the waveforms of the original reference phase and the attenuated phase using the value of $\delta t_{\text{ScS-S}}^*$ obtained by the IFM. **(b)** The Pearson correlation value R between measurements of $\delta t_{\text{ScS-S}}^*$ from the two methods as a function of minimum waveform similarity ($R_{\text{IFM}}^2 > R_{\text{C}}^2$). **(c)** The dataset for measurements with a minimum waveform similarity R_{C}^2 of 0.9, i.e. $R_{\text{IFM}}^2 > 0.9$. The dashed lines are the imposed condition that $\Delta t^* = |\delta t_{\text{WM}}^* - \delta t_{\text{IFM}}^*| < 3$ s.

291 taneous frequencies of both S and ScS are between 0.03–0.11 Hz, which excludes fewer than 20
 292 measurements in total (less than 0.02% of measurements). We take this as evidence that our choice
 293 of bandpass preserves the frequency spectra of the data whilst minimising noise.

294 3 Results

295 3.1 Preliminary data analysis

296 We measured δt^* between S and ScS using both IFM and WM (see Methods). Our final dataset is
 297 shown in Figure 5, separated into six event depth ranges from 75–200 to 600–700 km and plotted
 298 as a function of epicentral distance.

299 The most obvious feature of the data is that there is a significant amount of scatter in the
 300 measurements ($\sigma_{\text{noise}} \sim 3$ s) which does not vary with the threshold similarity of waveforms R_{C}^2 .
 301 We therefore average the values of differential attenuation and travel time residuals (corrected for
 302 attenuation) at the ScS bounce point on a quasi-equal area cell map of the CMB (Figure 6). The
 303 travel time residuals show the expected global scale pattern of LLSVPs, with ScS raypaths travelling
 304 through the LLSVPs being more delayed relative to S than predicted by PREM (Figure 6b).
 305 However, no such large scale features are immediately obvious for the measurements of differential

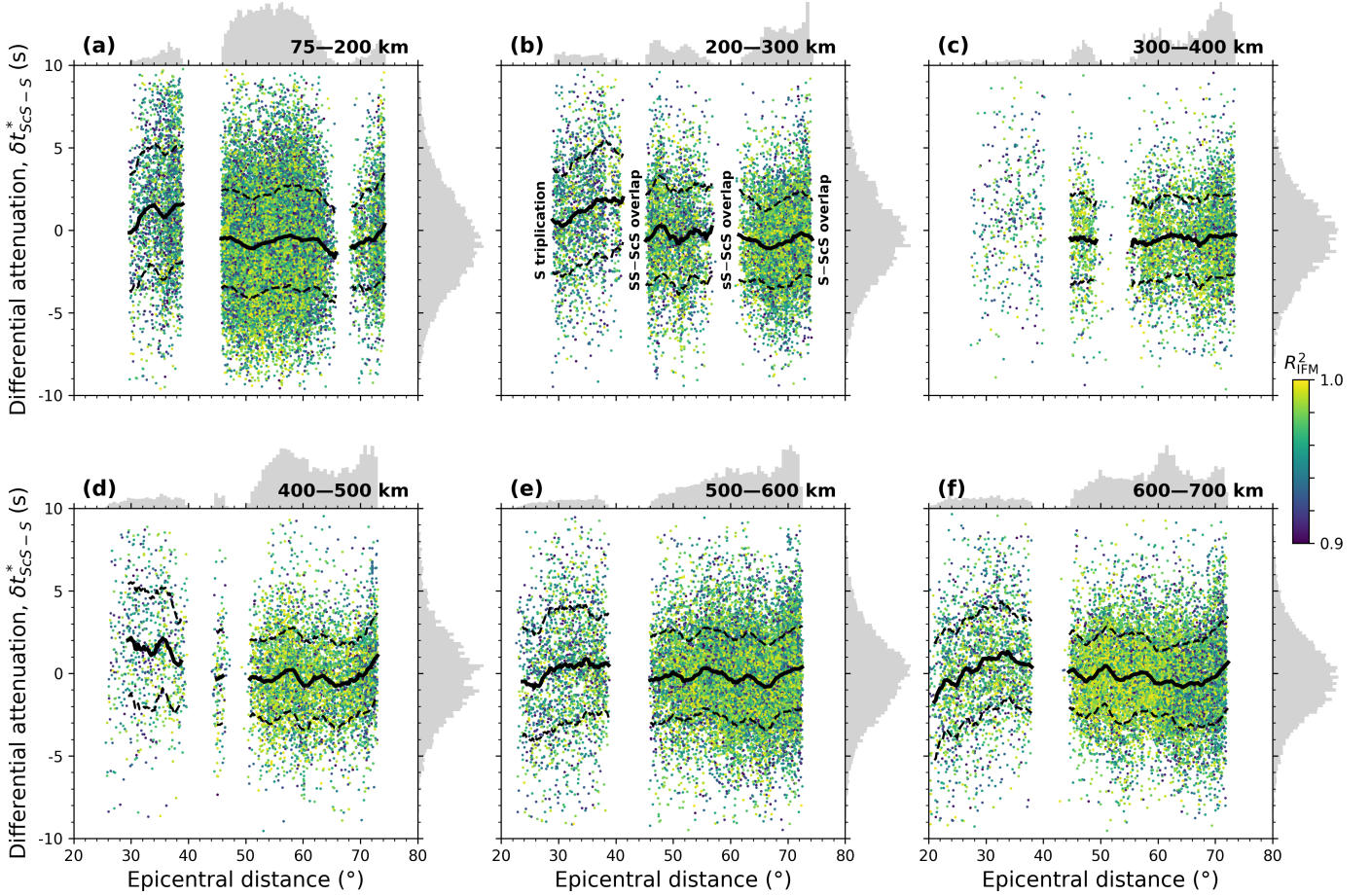


Figure 5: The mean value of differential attenuation $\delta t_{\text{ScS-S}}^*$ between the IFM and WM methods for each waveform within our dataset. The data are plotted in six event depth ranges: (a) 75–200, (b) 200–300, (c) 300–400, (d) 400–500, (e) 500–600, (f) 600–700 km. The colour of each data point is the waveform similarity R_{IFM}^2 between the attenuated phase and the reference phase calculated in the IFM method. The mean (solid black) and standard deviation (dashed black) of each depth range have been overlaid, using a 2° rolling window. Normalised histograms of the epicentral distance and differential attenuation values have been projected on the upper and right sides of the subplots, respectively, for each of the event depth ranges. The gaps in data are a result of SS and sS overlapping with ScS at shorter and longer epicentral distances, respectively.

306 attenuation (Figure 6a). We also plot the measurements of differential attenuation separated by
 307 turning depth of the S raypath in map view (Figure S3). In this representation, there is a clear
 308 global distribution of positive $\delta t_{\text{ScS-S}}^*$ between 800–1000 km turning depth of S (approximately
 309 $20\text{--}30^\circ$ epicentral distance), and a clear global distribution of negative $\delta t_{\text{ScS-S}}^*$ for turning depths
 310 1000–2000 km (where 2000 km is the deepest turning depth of S in our dataset, around 75° epicentral
 311 distance). That is to say, ScS is more attenuated than S between $20\text{--}30^\circ$ and S is more attenuated
 312 than ScS between $30\text{--}75^\circ$. This matches with the overall distribution of measured instantaneous

313 frequencies of S and ScS (Figure S4), $f_S = 72.1 \pm 9.0$ mHz and $f_{\text{ScS}} = 72.8 \pm 9.4$ mHz, which shows
 314 that on average S is more attenuated than ScS.

315 Before analysing the dataset further, we first benchmarked our aggregated observations (Figure
 316 7a) against other published datasets of $\delta t_{\text{ScS-S}}^*$ (Figure 7b). Lai et al. [2019] used waveform matching
 317 of empirical wavelets and Sun et al. [2025] used the instantaneous frequency matching method to
 318 estimate the absolute attenuation of shear phases relative to synthetics computed for tomographic
 319 model S40RTS [Ritsema et al., 2011]. From these datasets, we then constructed the relative at-
 320 tenuation if both measurements were available at a given event-station pair (for Lai et al. [2019])
 321 or epicentral distance (for Sun et al. [2025]). Lawrence and Wysession [2006] used the spectral
 322 ratio method to estimate the relative attenuation of ScS and S, which is directly comparable to our
 323 measurements, but is also the least consistent with our measurements. Whilst there are differences
 324 between the datasets, there are some reassuring similarities: (i) the relative attenuation is more
 325 positive at shorter epicentral distances than at longer epicentral distances; (ii) there is a consistent
 326 increase in relative attenuation between $65\text{--}75^\circ$; and (iii) a consistent minimum in relative atten-
 327 uation around $65\text{--}70^\circ$. However, there are clear offsets in the averages between datasets and also
 328 in the amplitude of our dataset compared to the others. It is difficult to ascertain whether this
 329 is due to lateral variations in the data sampling distributions or the accuracy of the measurement
 330 techniques used in the studies, or both.

331 **3.2 Forward modelling**

332 Since measurements of $\delta t_{\text{ScS-S}}^*$ represent the cumulative attenuation difference between two ray-
 333 paths, interpreting the data is not a straightforwardly intuitive process. Our first step was there-
 334 fore to perform forward modelling to establish how variations in Q_μ influence the predicted $\delta t_{\text{ScS-S}}^*$.
 335 Figure 8 shows how perturbations in Q_μ in different depth layers affect the predicted $\delta t_{\text{ScS-S}}^*$ as a
 336 function of epicentral distance. At shallow depths, from the surface to ~ 750 km depth, there is
 337 very little deviation from a uniform Q_μ for strong positive or negative perturbations due to the
 338 negligible difference between the S and ScS raypaths. Towards the bottom of the mantle, below
 339 ~ 2200 km depth, positive and negative perturbations in layers of the uniform Q_μ profile result in
 340 approximately linear negative and positive shifts in $\delta t_{\text{ScS-S}}^*$, respectively. This occurs due to ScS
 341 spending approximately the same time at each depth, which varies little with epicentral distance

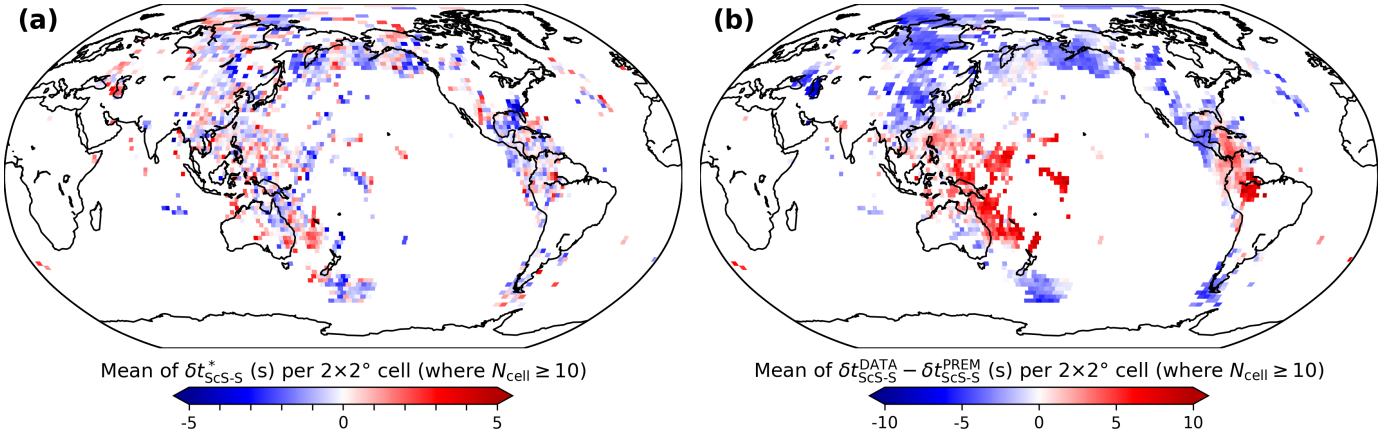


Figure 6: Mean values of (a) $\delta t_{\text{ScS-S}}^*$ and (b) $\delta t_{\text{ScS-S}}^{\text{DATA}} - \delta t_{\text{ScS-S}}^{\text{PREM}}$ per $2 \times 2^\circ$ quasi-equal area cell where grid cells with fewer than 10 ScS bounce points have been omitted.

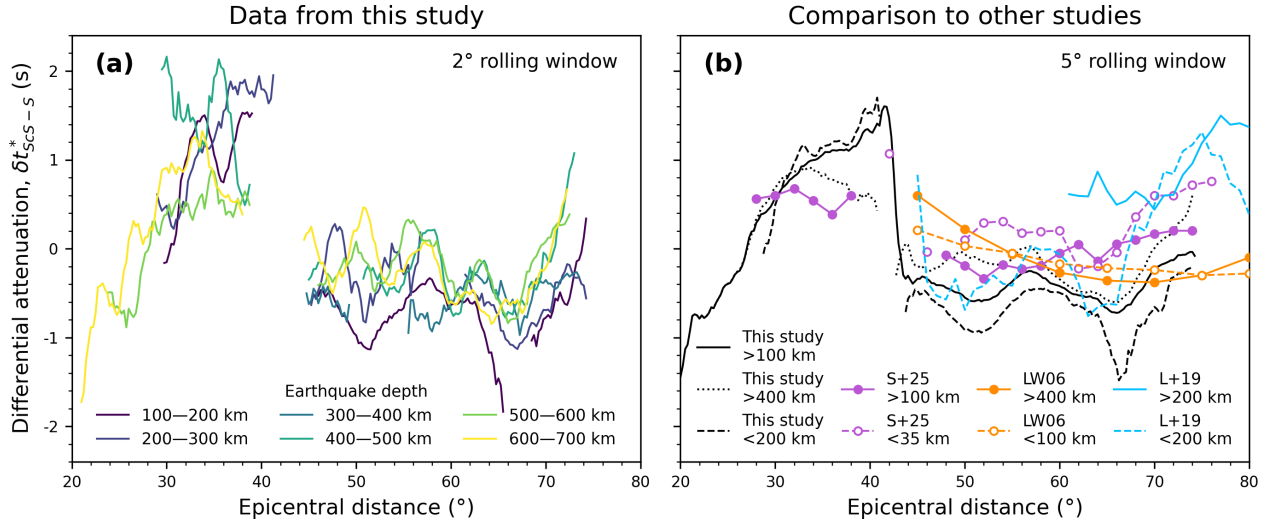


Figure 7: (a) The mean value of $\delta t_{\text{ScS-S}}^*$ for measurements in this study as a function of epicentral distance and earthquake depth, using a 2° rolling window. (b) Comparison of our dataset to other published datasets, using a 5° rolling window. Lawrence and Wyession [2006] made measurements of $\delta t_{\text{ScS-S}}^*$ for deep (> 400 km, solid orange) and shallow (< 100 km, dashed orange) earthquakes. Lai et al. [2019] made measurements of absolute attenuation for various phases; where two measurements were made for the same event-station pair, these were binned and averaged in the same way as our dataset but with a minimum threshold of 40 data per bin (blue). A comparison of the $\delta t_{\text{ScS-S}}^*$ values constructed from the dataset of Lai et al. [2019] to our dataset is shown in Figure S5. Sun et al. [2025] also made measurements of attenuation for a range of S and ScS multiples relative to PREM; estimates of $\delta t_{\text{ScS-S}}^*$ were constructed from the aggregated mean values for each of S and ScS for a 5° rolling window and uncorrected to PREM (purple).

342 (Figure S1a). However, at intermediate depths, between ~ 750 – 2200 km, there are strong non-linear
 343 effects, with some epicentral distance ranges shifted positively and others shifted negatively. We
 344 thus refer to our final model, which is a 1D model with sensitivity mostly to the mid-mantle region,
 345 as Q_{MID} . In a radially isotropic Earth, the relationship between the Q_{μ} profile with depth and
 346 resulting $\delta t_{\text{ScS-S}}^*$ with epicentral distance can therefore be approximately interpreted as a direct
 347 mapping, since the depth in the Q_{μ} profile is largely determined by the turning depth of the S
 348 raypath.

349 We include epicentral distances less than 40° despite potential triplication of S arrivals, as the
 350 waveforms are not strongly affected by this effect [e.g. Wang et al., 2018] and there are relatively
 351 few measurements at this epicentral distance range (Figure 5). Since we require WM and IFM
 352 to produce similar values, $\Delta t^* < 3$ s, and the attenuated waveform matches the unattenuated
 353 reference waveform, $R_C^2 = 0.9$, this likely has a negligible effect on our dataset. We also visually
 354 inspected S waveforms in this epicentral distance range for several events to confirm the absence
 355 of triplications. At epicentral distances much longer than 75° , the separation between S and ScS
 356 waveforms in the seismograms becomes too small to robustly interpret (Figure 1c).

357 **3.3 Inversion for 1D Q_{μ}**

358 We next perform an inversion for 1D Q_{μ} , in which we compute the forward model for earthquake
 359 depths of 100 to 700 km in intervals of 50 km and epicentral distances of 20 to 80° in intervals of
 360 0.5° . We then compute the misfit by comparing the measured $\delta t_{\text{ScS-S}}^*$ with the model corresponding
 361 to the nearest depth and epicentral distance of the event-station pair for the measurement. Before
 362 the inversion, we pre-compute the raypaths of S and ScS using TauP [Crotwell et al., 1999] through
 363 ObsPy [Beyreuther et al., 2010] for PREM, which makes each computation of the forward model
 364 extremely efficient. One full iteration – to compute $13 \times 121 = 1573$ forward models and the
 365 corresponding misfit for 90,000 measurements – takes on the order of 0.5 s on a single processor.
 366 As such, it becomes feasible to perform a Markov chain Monte Carlo (MCMC) inversion which
 367 is able to explore a wide parameter space and, most importantly, produce robust estimates of
 368 the associated uncertainties [e.g. Bodin and Sambridge, 2009]. Estimates of uncertainty derived
 369 from Bayesian inversion methodologies are also more reliable and realistic compared to those from
 370 linearised inversions [e.g. Rudolph et al., 2020], such as the one by Sun et al. [2025].

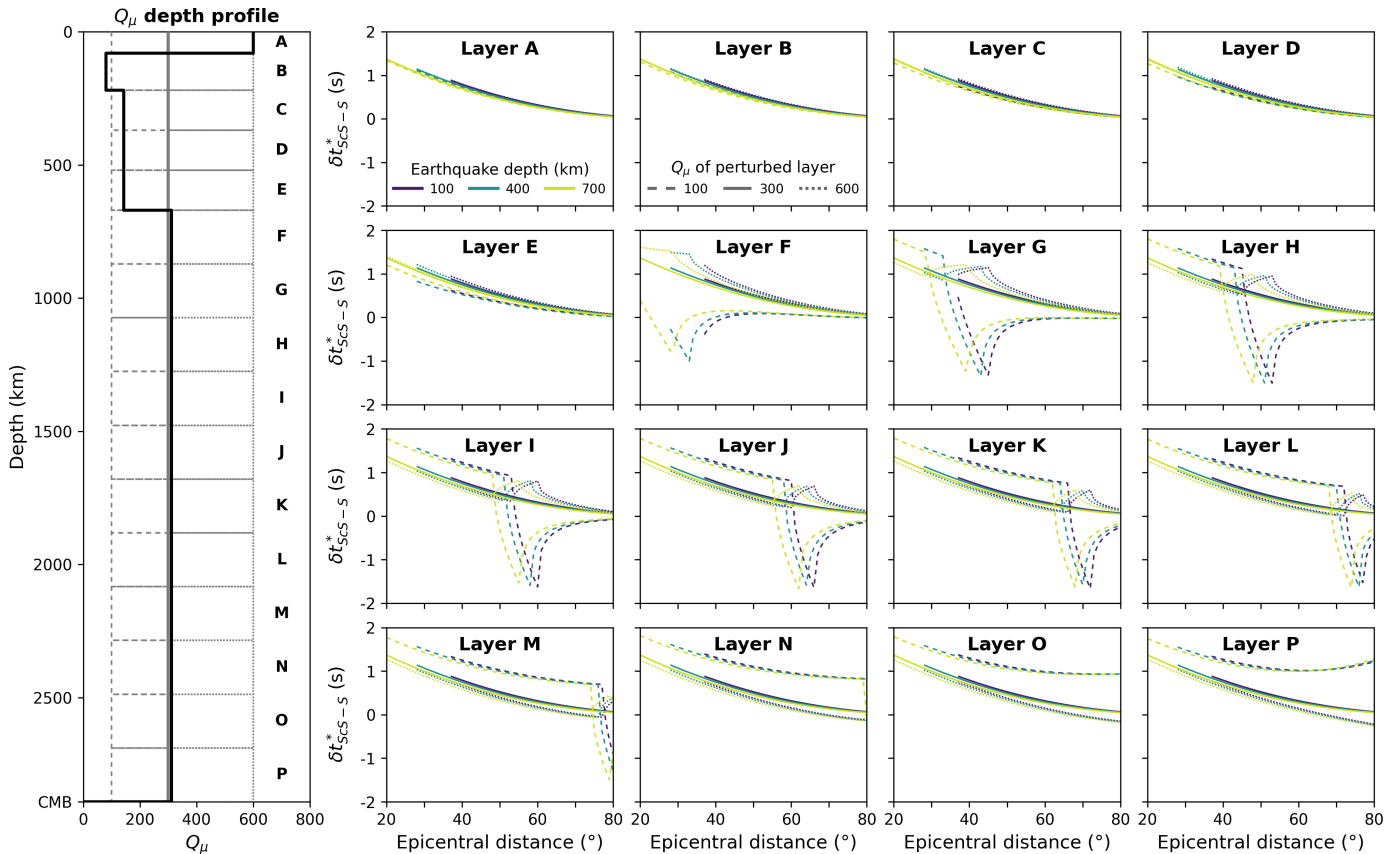


Figure 8: A depth profile (**left**) has been split up into 16 approximately equal-depth ranges and labelled **Layers A–P**. The Q_μ profile for PREM is plotted for reference (black line). Subplots (**right**) show the predicted $\delta t_{\text{ScS-S}}^*$ profiles as a function of epicentral distance for a perturbation in each layer only for event depths of 100 km (blue), 400 km (teal green) and 700 km (light green). The value of Q_μ in all other depth ranges is kept at 300. Each perturbed layer is allowed the value of 100 (dashed) or 600 (dotted), which is compared to a uniform profile of $Q_\mu = 300$ (solid).

371 We parameterise the Q_μ profile as a function of cubic B-splines in depth, such that

$$Q_\mu(r) = \sum_k p_k f_k(r) \quad (11)$$

372 where $f_k(r)$ are the cubic B-splines functions at radius r and p_k are the corresponding weighting
 373 factors of the basis functions. Since the weights of cubic B-splines are strictly positive, it means
 374 that all Q_μ profiles will be positive for $p_k > 0$. We thus allow p_k to vary between 1 and 1000
 375 (the prior distribution). From our initial analysis of the data, we expect a strongly heterogeneous
 376 region between 500–1000 km depth where our data shows strong variability. As such, we chose to
 377 use basis functions with 32 depth knots to ensure adequate depth resolution. For the uppermost

378 400 km, we use knots with fixed separation of 50 km with p_k chosen to be PREM-like, with the
 379 remaining knots distributed such that the spacing between nodes increases linearly down to the
 380 CMB (Figure 9a) following Sun et al. [2025].

381 The misfit $\Phi(m)$ of a model m of Q_μ is defined as

$$\Phi(m) = \sum_i \left(\frac{p_i(m) - d_i}{\sigma_{\text{noise}}} \right)^2 \quad (12)$$

382 where p is the predicted value of $\delta t_{\text{ScS-S}}^*$ for the model m , d is the observed value of $\delta t_{\text{ScS-S}}^*$, and σ_{noise}
 383 is the estimated value of the data noise (chosen as 5 s). This is larger than the standard deviation
 384 of the overall dataset of $\delta t_{\text{ScS-S}}^*$ measurements ($\sigma_{\text{noise}} \sim 3$ s), but this was chosen to ensure the
 385 parameter space was well explored in a manner similar to simulated annealing [e.g. Weber, 2000].
 386 For a proposed model m' , one randomly chosen weighting factor is perturbed by a step length
 387 drawn from a Gaussian distribution, $p'_k = p_k + \mathcal{N}(\Delta p_k)$. The forward model scheme is then run for
 388 the 1573 combinations of event depth and station epicentral distance using the proposed model,
 389 and the misfit is calculated for the dataset. The natural logarithm of the acceptance probability is
 390 [e.g. Bodin and Sambridge, 2009]

$$\ln [\alpha(m'|m)] = \min \left[0, \frac{1}{2} (\Phi(m') - \Phi(m)) \right] \quad (13)$$

391 The acceptance probability is then compared to a randomly drawn value $w = [0, 1)$: if $\alpha > w$
 392 the proposed model m' is accepted, otherwise it is rejected and a new proposal is drawn from the
 393 current model m . The form of the acceptance probability means that all proposed models which
 394 decrease the misfit are accepted, whilst those which increase the misfit can sometimes be accepted
 395 depending on the value of w . The posterior distribution, the probability distribution of Q_μ profiles
 396 which fit our dataset, is then taken to be the sparsely sampled distribution of models m after
 397 a sufficient burn in period to remove transient effects of the starting conditions [e.g. Bodin and
 398 Sambridge, 2009]. We find that for the setup presented here – 32 depth knots with the upper 6
 399 knots fixed to PREM-like values – the inversion converges after a burn in period of ~ 2000 iterations.
 400 The inversion ensemble is then taken as every 500th iteration from 50 parallel inversions after a
 401 burn in period of 2500 iterations and run for 12000 iterations. The ensemble distribution therefore

402 comprises of 1000 uncorrelated models from the posterior distribution, from which we calculate the
403 mean and standard deviation of each of the weighting factors p_k .

404 We also explored a range of other inversion setups, including:

- 405 1. Changing the number of depth knots and their relative separation (Figures S7 & S8). We
406 found that, regardless of the number of knots, the resulting Q_μ profile is very consistent
407 although the profiles with fewer knots led to broader features. 32 depth knots was a balance
408 between sufficient depth resolution and minimising overfitting noise.
- 409 2. Parameterising Q_μ in logarithmic space, similar to parameterisation used by Sun et al. [2025].
410 However, we found that this parameterisation was less stable due to the strong variations in
411 Q_μ required to fit our observed data unless we used a large number of depth splines.
- 412 3. Adding additional terms to the misfit if the predicted values of values of absolute attenuation
413 t_S^* were higher than those of PREM. This test was a result of recent measurements of absolute
414 attenuation of t_S^* which were approximately equal to or less attenuating than PREM synthetics
415 across all measured epicentral distances [Zhu et al., 2022; Sun et al., 2025].
- 416 4. Using different starting models to initiate the inversion. Due to the relatively high value of
417 σ_{noise} we use, the inversion was always well converged by ~ 2000 iterations for any uniform or
418 arbitrary starting models of Q_μ .

419 Our final model, Q_{MID} , is taken as the mean of the distribution of Q_μ profiles in the inversion
420 ensemble with the associated uncertainty in the model taken as the uncertainty in the weighting
421 factor of each depth knot (Figure 9b). Our model shows a strongly attenuating layer ($Q_\mu < 100$) at
422 750 km depth and two weakly attenuating layers ($Q_\mu \sim 600$) at 900 and 2000 km depth. Between the
423 two weakly attenuating layers, the mid-mantle is relatively strongly attenuating ($Q_\mu \sim 150 - 250$).
424 We then also compare our model to several previously published models (Figure 9c-d): PREM
425 [Dziewonski and Anderson, 1984], QM1 [Widmer et al., 1991], QL6 [Durek and Ekström, 1996],
426 QDW14 [De Wit et al., 2014], REM1D [Moulik and Ekström, 2025], QS4L3 [Talavera-Soza et al.,
427 2025], QLM9 [Lawrence and Wysession, 2006], QHR11 [Hwang and Ritsema, 2011], QMSF [Zhu
428 et al., 2022] and Q_{LID} [Sun et al., 2025]. PREM, QM1, QL6, QDW14, REM1D and QS4L3 are
429 constructed from measurements of quality factors of normal modes; whilst QLM9, QHR11, QMSF,

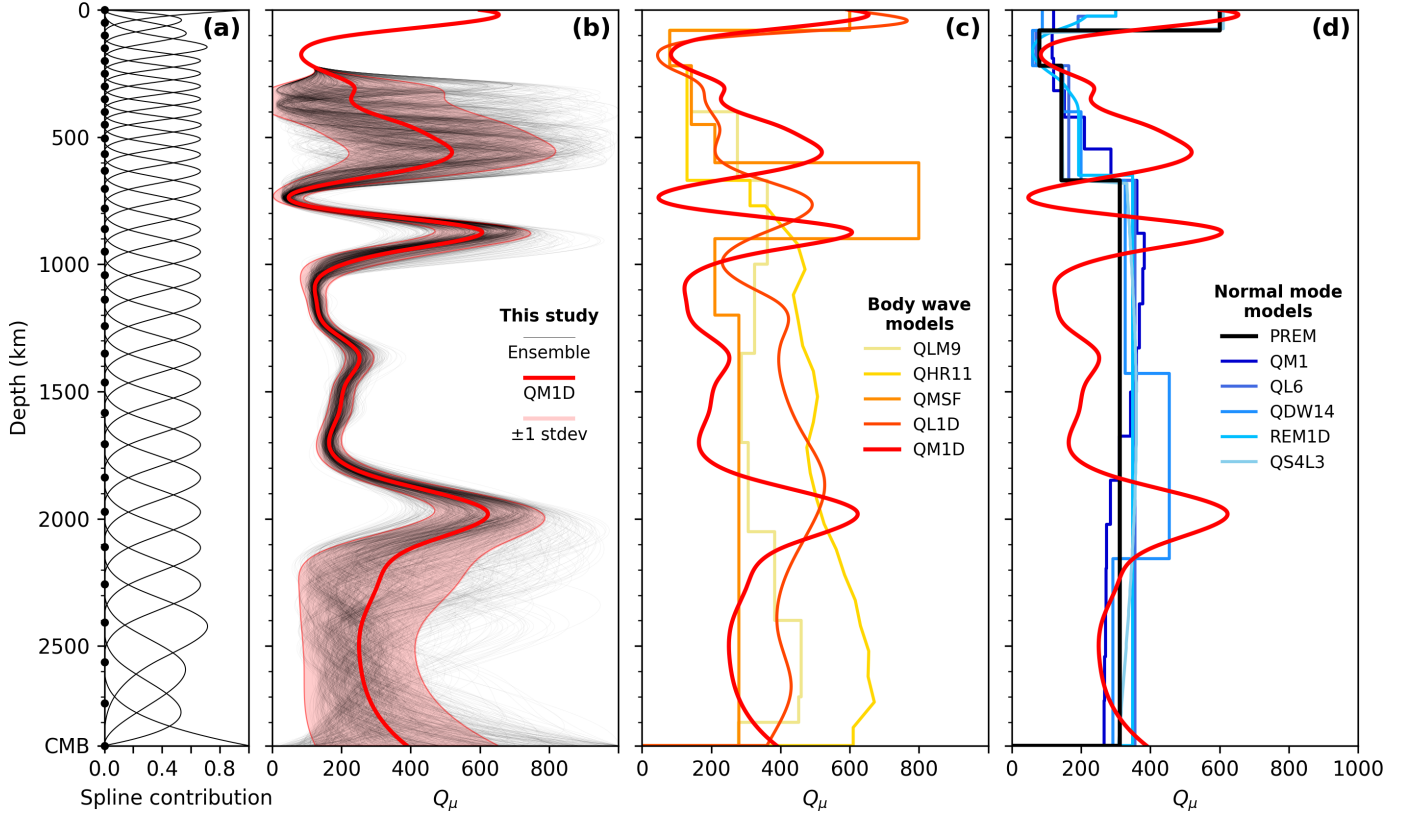


Figure 9: **(a)** The cubic B-splines of the basis functions used in our modelling with 32 depth knots. **(b)** The ensemble of models from our inversion (thin black lines), with the mean and standard deviation of the ensemble (red and pink, respectively). The mean of the ensemble is taken to be our model Q_{M1D} with its corresponding uncertainties for each depth parameter. A comparison of our model with **(c)** other short period body wave models (warm colours) and **(d)** various long period normal mode models (cool colours) of shear attenuation: black [PREM, Dziewonski and Anderson, 1984], dark blue [QM1, Widmer et al., 1991], blue [QL6, Durek and Ekström, 1996], medium blue [QDW14, De Wit et al., 2014], sky blue [REM1D, Moulik and Ekström, 2025], light blue [QS4L3, Talavera-Soza et al., 2025], pale yellow [QLM9, Lawrence and Wysession, 2006], yellow [QHR11, Hwang and Ritsema, 2011], orange [QMSF, Zhu et al., 2022], dark orange [Q_{L1D} , Sun et al., 2025], red [Q_{M1D} , this study].

430 Q_{L1D} and Q_{M1D} are from measurements of attenuation of body waves. Predictions of δt_{ScS-S}^* for
 431 these Q_μ profiles are plotted against the running average of our measurements, which show that
 432 only Q_{M1D} matches the trends in our dataset (Figure 10).

433 3.4 Comparison with other body wave lower mantle models

434 Our model Q_{M1D} differs significantly from previous models, notably around 500–1000 km depth.
 435 Whereas Zhu et al. [2022] and Sun et al. [2025] observe a weakly attenuating region around 750 km

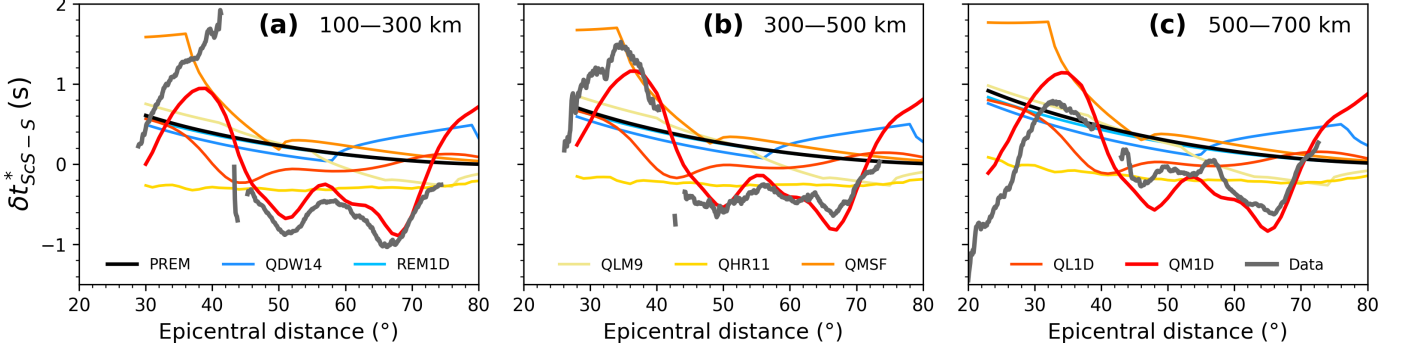


Figure 10: A comparison of predictions and observations of δt_{ScS-S}^* for a few different Q_μ profiles from Figure 9. Running averages of δt_{ScS-S}^* measurements are shown for event depth ranges (a) 100–300, (b) 300–500 and (c) 500–700 km, using a 5° rolling window (grey lines).

436 depth, our model prefers a thin strongly attenuating layer. There are also two very distinct low
 437 attenuation layers around 900 and 2000 km depth, the latter of which has not been robustly observed
 438 in any of the other models. These features in our Q_μ profile result in a significantly better fit to
 439 our dataset of δt_{ScS-S}^* measurements than any of the other models, which are broadly flat across
 440 the 20–80° epicentral distance range (Figure 10).

441 As well as direct comparisons between our observations of δt_{ScS-S}^* with those from other studies
 442 (Figure 7), we also compared our model Q_{M1D} to observations of other differential phase pairs, SS-S
 443 and SSS-SS, from previous studies (Figure S6a-d). Predictions from Q_{M1D} for these observations
 444 show a distinctly poor match, which is likely due to the poor resolution of the shallow mantle by the
 445 dataset we used to construct our model, but also due to the unmatched upper mantle and crustal
 446 contributions to the measurements for the differential phases. Similarly, several studies have found
 447 that their measurements are less attenuating than PREM, in contradiction with our results (Figure
 448 S6e-g). Zhu et al. [2022] find that, on average, the amplitudes of SS, SSS and SSSS phases are larger
 449 than those predicted in synthetics for PREM, implying that any model should be less attenuating
 450 than PREM overall. Hwang and Ritsema [2011] similarly found that their t_{data}^* was consistently
 451 below the predicted value of t_{PREM}^* for P and S waves. More recently, a similar analysis on a larger
 452 scale was completed by Sun et al. [2025] for S, SS, SSS, SSSS, ScS, ScS₂, ScS₃, Sdiff, and their
 453 respective depth phases. Whilst again there was a significant scatter in their data, there was a
 454 consistent trend that the phases were less attenuated than predicted by PREM. Sun et al. [2025]
 455 also suggested that there may be a low attenuation layer around 2000 km depth (although this

456 is not clear from their model Q_{L1D}). Indeed, adding a more pronounced weakly attenuation layer
457 in their preferred model Q_{L1D} at this depth improves the fit to their dataset of t_{SS}^* measurements
458 (Figure S6f).

459 Our model Q_{M1D} will also have important implications several previous studies which invert for
460 attenuation in the upper mantle using the assumption that the lower mantle contributes negligible
461 attenuation [e.g. Warren and Shearer, 2002; Souriau et al., 2012; Nguyen et al., 2025]. Several
462 studies have also assumed that a smoothly varying velocity profile from the base of the mantle
463 transition zone (MTZ) to the top of the D" region implies lack of strong attenuation heterogeneity
464 in this region [e.g. Flanagan and Wiens, 1994]. Our model therefore recommends caution to future
465 studies assuming that the effect of attenuation in the lower mantle can be neglected.

466 Zhao et al. [2015] investigated the Pacific region by creating an empirical source function for and
467 comparing the broadening of S. On average, as a function of epicentral distance, the S waves which
468 turned within the lowermost 900 km were more attenuating than S waves which turned around
469 900 km above the CMB. This matches with our observation of a low attenuation region around
470 2000 km (approximately 900 km above the CMB) with stronger attenuation below this depth. This
471 similarity could suggest that our observation of a low attenuation layer at 2000 km depth may be a
472 globally present feature, rather than just around the Pacific where our dataset is spatially biased.

473 3.5 Comparison with normal mode models

474 Nearly all Q_{μ} profiles derived from measurements of quality factors of long period normal mode
475 feature a roughly uniform weakly attenuating lower mantle with Q_{μ} between 300–400 [e.g. Dziewon-
476 ski and Anderson, 1981; Moulik and Ekström, 2025], except for QR05 [Resovsky et al., 2005] and
477 QDW14 [De Wit et al., 2014] which suggest that there is a weakly attenuating layer between 1500–
478 2000 km depth. In our model, we find a more strongly attenuating mid-mantle ($Q_{\mu} = 150$ –250),
479 flanked by two regions of low attenuation ($Q_{\mu} = 500$ –700). Given the poor depth resolution of
480 normal mode models [e.g. Talavera-Soza et al., 2025], most models are constructed using a very
481 coarse parameterisation of the lower mantle with the notable exception of QM1 [Widmer et al.,
482 1991]. It is therefore plausible that the weakly attenuating layer observed by Resovsky et al. [2005]
483 and De Wit et al. [2014] is the same as the one we find around 2000 km depth. The lowermost
484 600 km of the mantle in our model is also consistent with the long period Q_{μ} profiles, although we

485 note that Q_{MID} is poorly constrained in this region and there is a large uncertainty in our model
486 (Figure 9b). Finally, there do not appear to be any similarities between normal mode models and
487 a more attenuating mid-mantle or for a weakly attenuating layer at 900 km depth, as suggested by
488 Q_{MID} .

489 Attenuation is generally considered to be frequency dependent, i.e. $Q = Q_0 f^\alpha$ [e.g. Anderson
490 and Given, 1982], with a value of $\alpha \sim 0.1 - 0.3$ derived seismically [e.g. Lekić et al., 2009; Zaroli
491 et al., 2010; Romanowicz and Mitchell, 2015] and experimentally [e.g. Jackson and Faul, 2010;
492 McCarthy et al., 2011]. Over narrow frequency ranges, it is typically assumed that attenuation
493 is frequency independent – for example, this is an assumption of the spectral ratio method –
494 although Moulik and Ekström [2025] find that they do not need to invoke frequency dependence
495 of attenuation to satisfy observations over the range 1–3200 s period, i.e. $\alpha = 0$. If attenuation is
496 frequency dependent, Q_μ measured from body waves (higher frequency) would be expected to be
497 higher than those from normal modes (lower frequency) [e.g. Hwang and Ritsema, 2011; Sun et al.,
498 2025]. Assuming a dominant period of 300 s for the observations of normal modes and a uniform
499 layer of attenuation of the whole lower mantle with $Q_\mu = 312$ from PREM, we can compare this
500 with our model Q_{MID} from our dataset with a dominant period of 10–20 s to estimate values of α
501 at each depth range of the mantle. In the two layers of weak attenuation at 900 and 2000 km depth
502 we therefore obtain a value of α between 0.14 and 0.30, whilst in the mid-mantle between these
503 two layers α is between -0.27 and -0.07 . For the thin layer of strong attenuation at 750 km depth
504 and in the lowermost mantle, α is -0.75 to -0.48 and -0.08 to 0.04 , respectively. These values
505 are consistent with previously reported ranges [e.g. Lekić et al., 2009], including that attenuation is
506 independent of frequency in the lowermost mantle [e.g. Moulik and Ekström, 2025], except for the
507 highly negative values of α we observe for the strongly attenuating thin layer beneath the MTZ.

508 We also computed values of the Q of normal modes for both PREM and our model Q_{MID}
509 using MINEOS [Woodhouse, 1988; Masters et al., 2011] with all other parameters kept the same
510 as PREM, with the assumption that $\alpha = 0$. Comparing these predictions with the observed
511 measurements from normal modes [Deuss et al., 2013] (Figure S12), we find that there is relatively
512 good agreement between the different 1D profiles of Q_μ with the measurements, suggesting that a
513 heterogeneous joint model of normal mode and body wave observations may be possible.

514 4 Discussion

515 4.1 Uncertainty in the data and methodology

516 Various effects – such as de/focussing, anisotropy, and scattering – can cause a decrease in ampli-
517 tude or a broadening of seismic waveforms. Such effects result in a measured attenuation (‘apparent
518 attenuation’) which is larger than the true attenuation due to anelastic absorption of energy (‘in-
519 trinsic attenuation’) [e.g. Cormier, 2020]. In the following sections, we discuss these effects and the
520 potential influence they have on our observations and interpretations.

521 4.1.1 Effect of de/focussing of elastic structure

522 Chaves and Ritsema [2016] used synthetic modelling to demonstrate that measurements of ScS/ScS₂
523 amplitude ratios are dominated by focussing effects due to elastic structure, i.e. velocity, rather than
524 3D variations in attenuation. Similarly, Pang et al. [2023] found that focussing effects accounted
525 for up to 20% of the differential attenuation between station pairs of shallow events measured using
526 the spectral ratio method. However, they noted that the complex azimuthal patterns observed in
527 shallow events were almost non-apparent for events deeper than 150 km.

528 At short epicentral distances, the layered velocity structure in the upper mantle results in
529 triplication of S waves. This would likely lead to broadening of the S waveform and an apparent
530 increase in t_{ξ}^* and thus a more negative $\delta t_{\text{ScS-S}}^*$, which matches the trend in relative attenuation we
531 observed (Figure 5). However, our relative attenuation trend appears to be robust across all event
532 depths and extends well into epicentral distances for which triplications are not predicted (model
533 predictions are truncated in Figure 10 when triplications are predicted for PREM). Additionally,
534 the number of measurements at the shortest epicentral distances are far outnumbered by those at
535 longer epicentral distances (Figure 5) and so any trend in our data due to triplication will have a
536 weak effect on the misfit during the inversion process. Nonetheless, we only include data in the
537 misfit for which PREM does not predict a triplication in S, resulting in a final dataset of 90,000
538 $\delta t_{\text{ScS-S}}^*$ measurements from 894 events.

539 4.1.2 Effect of anisotropy

540 Presence of anisotropy in the mantle can also lead to the broadening of the SH phase, which could
541 be misinterpreted as being due to anelastic attenuation [Cormier, 2020]. Anisotropy is thought
542 only to be significant in the uppermost and lowermost mantle [e.g. Cormier, 2020]. Since S and
543 ScS have similar raypaths near to the receiver in the upper mantle, any potential broadening would
544 affect both phases and approximately cancel out. However, only ScS passes through the lowermost
545 mantle and so it is possible that there is a small contribution from anisotropy in this region to
546 broadening of ScS, resulting in a larger apparent differential attenuation between ScS and S (i.e.
547 more positive $\delta t_{\text{ScS-S}}^*$). When we compare our dataset with other published values, we find that our
548 average values of $\delta t_{\text{ScS-S}}^*$ are in fact more negative. Therefore, it is unlikely that anisotropy affects
549 our dataset noticeably. Indeed, Ford et al. [2012] and Durand et al. [2013] – who both investigated
550 the effect of correcting for anisotropy on measurements of deep earthquakes targetting the CMB
551 near Central America – concluded that the effect was small (on the order of tenths of a second)
552 and that corrections did not correlate with 3D velocity models. As such, we do not correct for any
553 potential waveform broadening caused by anisotropy in this study.

554 4.1.3 Effect of scattering

555 Elastic structure on the order of wavelength of the seismic waves can cause the elastic redistribution
556 (i.e. scattering) of energy which results in an effective pulse broadening and increase in apparent
557 attenuation or spectral holes in the signals [e.g. Cormier, 2020]. Since scattering is a redistribution
558 of energy, it should not be misinterpreted as anelastic attenuation which is absorption of energy.
559 Previous studies have found that, whilst such scatterers may broaden waveforms, this would require
560 significant variations in density and elastic parameters of 6–9%, which is much larger than observed
561 in tomographic models [e.g. Ricard et al., 2014]. Small-scale structure may be present in the mid-
562 mantle [e.g. Kaneshima, 2016; Waszek et al., 2018], which would result in more scattering of S than
563 ScS on average and therefore lead to the more negative values of $\delta t_{\text{ScS-S}}^*$ we observe. However, most
564 seismic observations of scatterers have been located within or near the D'' layer in the lowermost
565 mantle [e.g. Shearer, 2007; Rost et al., 2015; Rost and Frost, 2025] and there are significantly fewer
566 studies which suggest there are small-scale scatterers in the mid-mantle. Therefore, since scatterers

567 in the D” would only affect ScS, which would result in a more negative $\delta t_{\text{ScS-S}}^*$, it seems unlikely that
568 scattering has had a significant impact on our measurements. Various studies have attempted to
569 distinguish between intrinsic attenuation and scattering from apparent attenuation using radiative
570 transfer theory [e.g. Fehler et al., 1992; Carcolé and Sato, 2010; Ogiso, 2019; Akande et al., 2019],
571 but this is beyond the scope of this paper.

572 4.2 Comparison to mineralogy

573 Whilst in the upper 400 km of the mantle there is increasing evidence for an anti-correlation
574 between 3D models of shear velocity and attenuation [e.g. Romanowicz, 1995; Dalton et al., 2008;
575 Karaoğlu and Romanowicz, 2018; Talavera-Soza et al., 2025] – suggestive of related causal physical
576 mechanisms such as temperature, grain size, water content or partial melt [e.g. Jackson et al., 2002]
577 – there does not appear to be any similar correlation between 1D models of shear velocity and
578 attenuation in the lower mantle. We compared our observations of differential attenuation $\delta t_{\text{ScS-S}}^*$
579 with shear wave velocity variations (V_S) from 3D tomographic models SEMUCB-WM1 [French and
580 Romanowicz, 2014], REVEAL [Thrustarson et al., 2024] and GLAD-M35 [Cui et al., 2024] at the
581 turning point of S (Figure S9) and at the bounce point of ScS (Figure S10) of our dataset. There is
582 a weak anti-correlation between shear velocity at the turning point of S with differential attenuation
583 ($R \sim -0.08$) and a weaker anti-correlation between shear velocity at the bounce point of ScS with
584 differential attenuation ($R \sim -0.03$). The strongest – but still weak – anti-correlation is found
585 between travel time residuals between observed and predicted $\delta t_{\text{ScS-S}}$ and differential attenuation
586 (Figure S11, $R \sim -0.09$), which suggests that there is no coupled dominant physical mechanism
587 driving perturbations in velocity and attenuation in the lower mantle.

588 Previous studies have interpreted low attenuation layers in their Q_μ profiles as evidence for
589 regions of high viscosity [Lawrence and Wysession, 2006; Sun et al., 2025] (Figure 11). Several
590 studies have found evidence for an increase in viscosity in the mantle around 1000 km depth from
591 geodynamical modelling [e.g. Kido and Čadek, 1997; Forte and Mitrovica, 2001; Höink et al., 2012;
592 Rudolph et al., 2015], experimental mineralogy [e.g. Marquardt and Miyagi, 2015], and seismic to-
593 mography [e.g. Fukao and Obayashi, 2013; French and Romanowicz, 2015]. Some have additionally
594 identified an increase in viscosity around 2000 km depth [e.g. Ricard and Wuming, 1991; Forte
595 and Mitrovica, 2001; Forte et al., 2010; Brown et al., 2026], matching our observation of a low

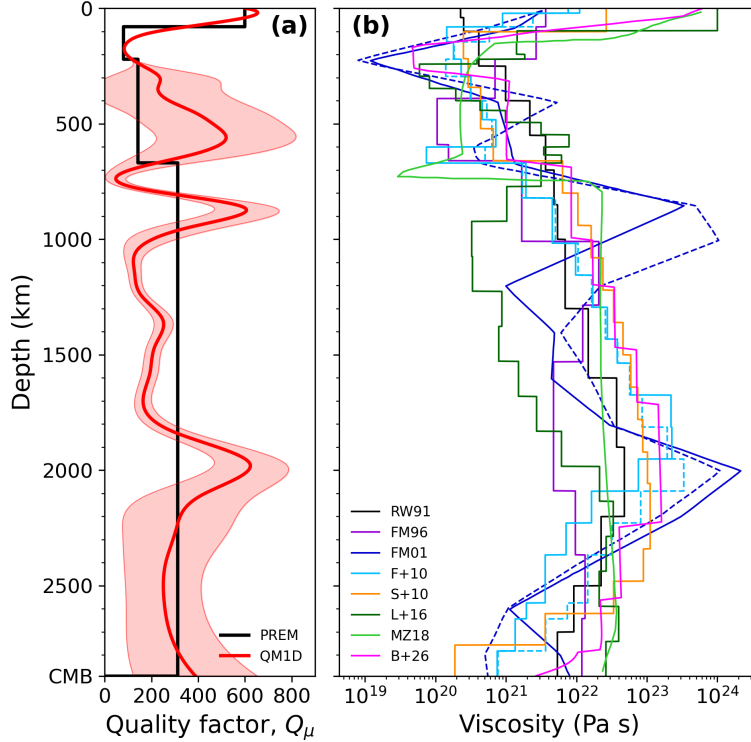


Figure 11: A comparison of radial profiles of (a) shear Q_μ for PREM and Q_{MID} with (b) mantle viscosity: black [Ricard and Wuming, 1991], purple [Forte and Mitrovica, 1996], dark blue [Forte and Mitrovica, 2001], light blue [Forte et al., 2010], orange [Steinberger et al., 2010], dark green [Lau et al., 2016], light green [Mao and Zhong, 2018] and pink [Brown et al., 2026]. Dashed lines indicate alternative models.

596 attenuation layer at this depth, which Glišović et al. [2015] interpreted as the region of maximum
 597 grain size within the mantle. The thin highly attenuating layer in our model at 750 km depth is
 598 also consistent with previous suggestions of a thin low viscosity layer at the bottom of the MTZ
 599 which is thought to potentially control slab stagnation [e.g. Mitrovica and Forte, 2004; Mao and
 600 Zhong, 2018; Rudolph et al., 2020], although evidence for this is mixed [e.g. Liu et al., 2021]. Mao
 601 and Zhong [2021] further find that geodynamic models with a thin layer beneath the MTZ only in
 602 regions of slab subduction can explain observed slab stagnation equally well as geodynamic models
 603 including a global layer, which may explain why the layer is distinctly visible in our model (with
 604 data coverage predominantly in regions of subduction, Figure 2b) but not in others, e.g. Q_{LID} .

605 4.3 Future developments and suggestions

606 ScS-S is fundamentally limited by the source-receiver geometries for which ScS can be measured
607 without being contaminated by other phases (Figure 1b), resulting in a spatial sampling biased
608 around the edge of the Pacific (Figure 2b). Other studies which have addressed the problem of
609 spatial bias have typically measured absolute attenuation values of different shear phases [e.g. Lai
610 et al., 2019; Zhu et al., 2022; Sun et al., 2025]. However, measuring the absolute attenuation is
611 difficult and involves strong assumptions about the attenuation contributions from the source and
612 receiver regions [Sun et al., 2025]. As such, other pairs of differential phases are required to increase
613 the spatial sampling and ensure less uncertainty in measurements of δt^* . ScSScS and SS may be one
614 such potential avenue to increase the spatial sampling of our dataset. While this phase combination
615 will still have the same constraints of depth sensitivity – i.e. predominantly the mid-mantle – it
616 would have a more global distribution than the spatially biased $\delta t^*_{\text{ScS-S}}$ dataset we present in this
617 study. Such improvements in spatial sampling are required to make progress towards a 3D model
618 of attenuation of the mantle from body waves.

619 Figure S7 shows the inversion results for a number of different depth splines with 24, 32, 50 and
620 90 knots for comparison with the 32 knots we used in our new model, Q_{MID} . We recommend any
621 future study using a spline parameterisation for Q_{μ} to implement an irregularly spaced arrangement
622 of knots to ensure sufficient resolution around the 900 and 2000 km layers of low attenuation and
623 the 750 km depth layer of high attenuation. Alternatively, it may be preferable to perform a
624 transdimensional MCMC in which the number of knots is also an unknown variable [e.g. Bodin and
625 Sambridge, 2009], but this would create additional computational challenges if the objective is a
626 3D model of attenuation.

627 5 Conclusions

628 Using a dataset of 90,000 high-quality measurements of differential attenuation between S and ScS
629 body waves, we have constructed a new 1D model of shear attenuation Q_{μ} in the mantle, Q_{MID} .
630 We find a thin strongly attenuating layer around 750 km depth, and two weakly attenuating layers
631 at 900 and 2000 km depth. We speculate that key features in our attenuation profile are related to
632 features observed in viscosity profiles of the mantle. The low attenuation layers at 900 and 2000 km

633 depth could be related to increases in global viscosity in the deep mantle, and the high attenuation
634 layer at 750 km depth could be related to a thin layer of low viscosity beneath the mantle transition
635 zone in the presence of subducted slab material. Our model also suggests the mid-mantle is more
636 attenuating than usually assumed from models based on normal modes, including the widely-used
637 1D reference model PREM.

638 **Acknowledgements**

639 CM and AD were funded by a Vici award (grant number 016.160.310/526) from the Dutch Research
640 Council (NWO). The computational facility at Utrecht, Eejit, was used to perform the analysis in
641 this work. We thank Hanneke Paulssen, Stuart Russell, Jochem Veerman, Michael Koch, Lauren
642 Waszek, Mark Hoggard, Thomas Duvernay and Hamish Brown for helpful discussions and Lukas
643 van de Wiel for technical support.

644 **Data and code availability**

645 The facilities of IRIS Data Services (www.iris.edu) were used to download waveforms and related
646 metadata. IRIS Data Services are funded through the Seismological Facilities for the Advance-
647 ment of Geoscience (SAGE) Award of the National Science Foundation under Cooperative Support
648 Agreement EAR-1851048. Data were downloaded from data centres EarthScope, GFZ, NOA, RE-
649 SIF, ORFEUS, GeoNet, AusPass, USP, KOERI and UIB-NORSAR. Additionally, data from the
650 F-net network were made available by National Research Institute for Earth Science and Disaster
651 Resilience [Okada et al., 2004]. Data from NIED was downloaded using HinetPy [Tian, 2024].
652 Earthquake parameters were used from the Global CMT Project (www.globalcmt.org). We used
653 TauP [Crotwell et al., 1999] and ObsPy [Beyreuther et al., 2010] to do the analysis in this project,
654 and matplotlib [Hunter, 2007] and basemap (<https://matplotlib.org/basemap/>) to make the figures.
655 Codes and datasets will be made available on GitHub and Zenodo upon publication.

656 **Competing interests**

657 Authors declare that they have no competing interests.

References

- 658
- 659 Adenis, A., Debayle, E. and Ricard, Y. [2017], ‘Attenuation tomography of the upper mantle’,
660 **44**(15), 7715–7724.
- 661 Akande, W. G., De Siena, L. and Gan, Q. [2019], ‘Three-dimensional kernel-based coda attenu-
662 ation imaging of caldera structures controlling the 1982-84 Campi Flegrei unrest’, *Journal of*
663 *Volcanology and Geothermal Research* **381**, 273–283.
- 664 Aki, K. and Richards, P. G. [2002], *Quantitative seismology*, MIT Press.
- 665 Anderson, D. L. and Given, J. W. [1982], ‘Absorption band Q model for the Earth’, *Journal of*
666 *Geophysical Research: Solid Earth* **87**(B5), 3893–3904.
- 667 Asada, T. and Takano, K. [1963], ‘Attenuation of short period P waves in the mantle’, *Journal of*
668 *Physics of the Earth* **11**(1), 25–34.
- 669 Barnes, A. E. [1993], ‘Instantaneous spectral bandwidth and dominant frequency with applications
670 to seismic reflection data’, *Geophysics* **58**(3), 419–428.
- 671 Bernard, P., Herrero, A. and Berge, C. [1996], ‘Modeling directivity of heterogeneous earthquake
672 ruptures’, *Bulletin of the Seismological Society of America* **86**(4), 1149–1160.
- 673 Beyreuther, M., Barsch, R., Krischer, L., Megies, T., Behr, Y. and Wassermann, J. [2010], ‘ObsPy:
674 A Python toolbox for seismology’, *Seismological Research Letters* **81**(3), 530–533.
- 675 Bezada, M. J., Byrnes, J. S., Zhu, Z. and Lee, H. [2023], ‘Lateral Variations in Teleseismic At-
676 tenuation of the Conterminous U.S. and New Insights Derived From Its Relationship to Mantle
677 Seismic Velocity’, *Journal of Geophysical Research: Solid Earth* **128**(12), e2023JB027299.
678 **URL:** <https://agupubs.onlinelibrary.wiley.com/doi/abs/10.1029/2023JB027299>
- 679 Bhattacharyya, J. [1998], ‘Comparison between time-domain and frequency-domain measurement
680 techniques for mantle shear-wave attenuation’, *pure and applied geophysics* **153**(2), 399–417.
- 681 Bhattacharyya, J., Masters, G. and Shearer, P. [1996], ‘Global lateral variations of shear wave
682 attenuation in the upper mantle’, *Journal of Geophysical Research: Solid Earth* **101**(B10), 22273–
683 22289.

- 684 Bodin, T. and Sambridge, M. [2009], ‘Seismic tomography with the reversible jump algorithm’,
685 *Geophysical Journal International* **178**(3), 1411–1436.
686 **URL:** <https://doi.org/10.1111/j.1365-246X.2009.04226.x>
- 687 Borgeaud, A. F. and Deschamps, F. [2021], ‘Seismic Attenuation and S-Velocity Structures in
688 Beneath Central America Using 1-D Full-Waveform Inversion’, *Journal of Geophysical Research:*
689 *Solid Earth* **126**(7), e2020JB021356.
- 690 Brown, H., Robl, G., Stotz, I., Vilacis, B., Chen, Y.-W., Hoggard, M., Schuberth, B., Bunge,
691 H.-P. and Oeser, J. [2026], ‘Constraining mantle viscosity using dynamic topography, the geoid,
692 and seismic heterogeneity from high-resolution mantle circulation models’, *Geophysical Journal*
693 *International* .
- 694 Brune, J. N. [1970], ‘Tectonic stress and the spectra of seismic shear waves from earthquakes’,
695 *Journal of Geophysical Research* **75**(26), 4997–5009.
- 696 Cao, A. and Romanowicz, B. [2004], ‘Hemispherical transition of seismic attenuation at the top of
697 the Earth’s inner core’, *Earth and Planetary Science Letters* **228**(3), 243–253.
698 **URL:** <https://www.sciencedirect.com/science/article/pii/S0012821X04005862>
- 699 Carcolé, E. and Sato, H. [2010], ‘Spatial distribution of scattering loss and intrinsic absorption of
700 short-period S waves in the lithosphere of Japan on the basis of the Multiple Lapse Time Window
701 Analysis of Hi-net data’, *Geophysical Journal International* **180**(1), 268–290.
- 702 Chan, W. W. and Der, Z. A. [1988], ‘Attenuation of multiple ScS in various parts of the world’,
703 *Geophysical Journal International* **92**(2), 303–314.
- 704 Chapman, C., Jen-Yi, C., Lyness, D. and Doornbos, D. [1988], ‘The WKBJ seismogram algorithm’,
705 *Seismological algorithms: Computational methods and computer programs* pp. 47–74.
- 706 Chaves, C. A. and Ritsema, J. [2016], ‘The influence of shear-velocity heterogeneity on ScS₂/ScS
707 amplitude ratios and estimates of Q in the mantle’, *Geophysical Research Letters* **43**(15), 7997–
708 8005.
- 709 Cooper, R. F. [2002], ‘Seismic wave attenuation: Energy dissipation in viscoelastic crystalline
710 solids’, *Reviews in mineralogy and geochemistry* **51**(1), 253–290.

Cormier, V. F. [2020], *Seismic Viscoelastic Attenuation*, Springer International Publishing, Cham, pp. 1–14.

URL: https://doi.org/10.1007/978-3-030-10475-7_5 – 1

- 711 Croswell, H. P., Owens, T. J., Ritsema, J. et al. [1999], ‘The TauP Toolkit: Flexible seismic travel-
712 time and ray-path utilities’, *Seismological Research Letters* **70**, 154–160.
- 713 Cui, C., Lei, W., Liu, Q., Peter, D., Bozdağ, E., Tromp, J., Hill, J., Podhorszki, N. and Pugmire, D.
714 [2024], ‘GLAD-M35: a joint P and S global tomographic model with uncertainty quantification’,
715 *Geophysical Journal International* **239**(1), 478–502.
- 716 Dalton, C. A. and Ekström, G. [2006], ‘Global models of surface wave attenuation’, *Journal of*
717 *Geophysical Research: Solid Earth* **111**(B5).
- 718 Dalton, C. A., Ekström, G. and Dziewoński, A. M. [2008], ‘The global attenuation structure of the
719 upper mantle’, *Journal of Geophysical Research: Solid Earth* **113**(B9).
- 720 Dasios, A., Astin, T. and McCann, C. [2001], ‘Compressional-wave Q estimation from full-waveform
721 sonic data’, *Geophysical Prospecting* **49**(3), 353–373.
- 722 De Wit, R., Käuffl, P., Valentine, A. and Trampert, J. [2014], ‘Bayesian inversion of free oscillations
723 for Earth’s radial (an)elastic structure’, *Physics of the Earth and Planetary Interiors* **237**, 1–17.
- 724 Der, Z. A. and Lees, A. C. [1985], ‘Methodologies for estimating $t^*(f)$ from short-period body
725 waves and regional variations of $t^*(f)$ in the United States’, *Geophysical Journal International*
726 **82**(1), 125–140.
- 727 Deuss, A., Ritsema, J. and van Heijst, H. [2013], ‘A new catalogue of normal-mode splitting function
728 measurements up to 10 mHz’, *Geophysical Journal International* **193**(2), 920–937.
- 729 Durand, S., Matas, J., Ford, S., Ricard, Y., Romanowicz, B. and Montagner, J.-P. [2013], ‘Insights
730 from ScS–S measurements on deep mantle attenuation’, *Earth and Planetary Science Letters*
731 **374**, 101–110.
- 732 Durek, J. J. and Ekström, G. [1996], ‘A radial model of anelasticity consistent with long-period
733 surface-wave attenuation’, *Bulletin of the Seismological Society of America* **86**(1A), 144–158.

- 734 Dziewonski, A. M. and Anderson, D. L. [1981], ‘Preliminary reference Earth model’, *Physics of the*
735 *Earth and Planetary Interiors* **25**(4), 297–356.
- 736 Dziewonski, A. M. and Anderson, D. L. [1984], ‘Seismic Tomography of the Earth’s Interior: The
737 first three-dimensional models of the Earth’s structure promise to answer some basic questions
738 of geodynamics and signify a revolution in earth science’, *American Scientist* **72**(5), 483–494.
- 739 Eberhart-Phillips, D. and Chadwick, M. [2002], ‘Three-dimensional attenuation model of the shal-
740 low Hikurangi subduction zone in the Raukumara Peninsula, New Zealand’, *Journal of Geophys-*
741 *ical Research: Solid Earth* **107**(B2), ESE 3–1–ESE 3–15.
742 **URL:** <https://agupubs.onlinelibrary.wiley.com/doi/abs/10.1029/2000JB000046>
- 743 Eilon, Z. C. and Abers, G. A. [2017], ‘High seismic attenuation at a mid-ocean ridge reveals the
744 distribution of deep melt’, *Science Advances* **3**(5), e1602829.
745 **URL:** <https://www.science.org/doi/abs/10.1126/sciadv.1602829>
- 746 Faul, U. H. and Jackson, I. [2015], ‘Transient creep and strain energy dissipation: An experimental
747 perspective’, **43**, 541–569.
- 748 Fehler, M., Hoshihara, M., Sato, H. and Obara, K. [1992], ‘Separation of scattering and intrinsic
749 attenuation for the Kanto-Tokai region, Japan, using measurements of S-wave energy versus
750 hypocentral distance’, *Geophysical Journal International* **108**(3), 787–800.
- 751 Fisher, J. L., Wysession, M. E. and Fischer, K. M. [2003], ‘Small-scale lateral variations in D
752 attenuation and velocity structure’, *Geophysical research letters* **30**(8).
- 753 Flanagan, M. P. and Wiens, D. A. [1994], ‘Radial upper mantle attenuation structure of inactive
754 back arc basins from differential shear wave measurements’, *Journal of Geophysical Research:*
755 *Solid Earth* **99**(B8), 15469–15485.
756 **URL:** <https://agupubs.onlinelibrary.wiley.com/doi/abs/10.1029/94JB00804>
- 757 Ford, S. R., Garnero, E. J. and Thorne, M. S. [2012], ‘Differential t^* measurements via instanta-
758 neous frequency matching: observations of lower mantle shear attenuation heterogeneity beneath
759 western central america’, *Geophysical Journal International* **189**(1), 513–523.

- 760 Forte, A. M. and Mitrovica, J. X. [1996], ‘New inferences of mantle viscosity from joint inversion of
761 long-wavelength mantle convection and post-glacial rebound data’, *Geophysical Research Letters*
762 **23**(10), 1147–1150.
- 763 Forte, A. M. and Mitrovica, J. X. [2001], ‘Deep-mantle high-viscosity flow and thermochemical
764 structure inferred from seismic and geodynamic data’, *Nature* **410**(6832), 1049–1056.
- 765 Forte, A. M., Quéré, S., Moucha, R., Simmons, N. A., Grand, S. P., Mitrovica, J. X. and Rowley,
766 D. B. [2010], ‘Joint seismic–geodynamic–mineral physical modelling of African geodynamics: A
767 reconciliation of deep-mantle convection with surface geophysical constraints’, *Earth and Plane-
768 tary Science Letters* **295**(3-4), 329–341.
- 769 French, S. and Romanowicz, B. A. [2014], ‘Whole-mantle radially anisotropic shear velocity struc-
770 ture from spectral-element waveform tomography’, **199**(3), 1303–1327.
- 771 French, S. W. and Romanowicz, B. [2015], ‘Broad plumes rooted at the base of the Earth’s mantle
772 beneath major hotspots’, *Nature* **525**(7567), 95–99.
- 773 Fukao, Y. and Obayashi, M. [2013], ‘Subducted slabs stagnant above, penetrating through,
774 and trapped below the 660 km discontinuity’, *Journal of Geophysical Research: Solid Earth*
775 **118**(11), 5920–5938.
- 776 Garcia, R., Schardong, L. and Chevrot, S. [2013], ‘A nonlinear method to estimate source paramete-
777 rs, amplitude, and travel times of teleseismic body waves’, *Bulletin of the Seismological Society
778 of America* **103**(1), 268–282.
- 779 Glišović, P., Forte, A. M. and Ammann, M. W. [2015], ‘Variations in grain size and viscosity
780 based on vacancy diffusion in minerals, seismic tomography, and geodynamically inferred mantle
781 rheology’, *Geophysical Research Letters* **42**(15), 6278–6286.
- 782 Gomer, B. and Okal, E. [2003], ‘Multiple-ScS probing of the Ontong-Java plateau’, *Physics of the
783 Earth and Planetary Interiors* **138**(3-4), 317–331.
- 784 Gung, Y. and Romanowicz, B. [2004], ‘Q tomography of the upper mantle using three-component
785 long-period waveforms’, *Geophysical Journal International* **157**(2), 813–830.

786 Hansen, S. E., Garnero, E. J. and Rost, S. [2021], ‘Historical interstation pattern referencing
787 (HIPR): An application to PcP waves recorded in the Antarctic for ULVZ imaging’, *Journal of*
788 *Geophysical Research: Solid Earth* **126**(10), e2021JB022741.

789 Hunter, J. D. [2007], ‘Matplotlib: A 2D graphics environment’, *Computing in Science & Engineering*
790 **9**(3), 90–95.

791 Hwang, Y. K. and Ritsema, J. [2011], ‘Radial Q_μ structure of the lower mantle from teleseismic
792 body-wave spectra’, *Earth and Planetary Science Letters* **303**(3-4), 369–375.

793 Hwang, Y. K., Ritsema, J. and Goes, S. [2009], ‘Spatial variations of P wave attenuation in the
794 mantle beneath North America’, *Journal of Geophysical Research: Solid Earth* **114**(B6).

795 Höink, T., Lenardic, A. and Richards, M. [2012], ‘Depth-dependent viscosity and mantle stress
796 amplification: implications for the role of the asthenosphere in maintaining plate tectonics’,
797 *Geophysical Journal International* **191**(1), 30–41.
798 **URL:** <https://doi.org/10.1111/j.1365-246X.2012.05621.x>

799 Isse, T. and Nakanishi, I. [1997], ‘The effect of the crust on the estimation of mantle Q from spectral
800 ratios of multiple ScS phases’, *Bulletin of the Seismological Society of America* **87**(3), 778–781.

801 Jackson, I. and Faul, U. H. [2010], ‘Grainsize-sensitive viscoelastic relaxation in olivine: Towards a
802 robust laboratory-based model for seismological application’, *Physics of the Earth and Planetary*
803 *Interiors* **183**(1-2), 151–163.

804 Jackson, I., Fitz Gerald, J. D., Faul, U. H. and Tan, B. H. [2002], ‘Grain-size-sensitive seis-
805 mic wave attenuation in polycrystalline olivine’, *Journal of Geophysical Research: Solid Earth*
806 **107**(B12), ECV–5.

807 Jackson, I., Paterson, M. and Fitz Gerald, J. [1992], ‘Seismic wave dispersion and attenuation in
808 Åheim dunite: an experimental study’, *Geophysical Journal International* **108**(2), 517–534.

809 Kanamori, H. and Rivera, L. [2015], ‘Near-vertical multiple ScS phases and vertically averaged
810 mantle properties’, *Geological Society of America Special Papers* .

- 811 Kaneshima, S. [2016], ‘Seismic scatterers in the mid-lower mantle’, *Physics of the Earth and Plan-*
812 *etary Interiors* **257**, 105–114.
- 813 **URL:** <https://www.sciencedirect.com/science/article/pii/S0031920116300620>
- 814 Karaoğlu, H. and Romanowicz, B. [2018], ‘Inferring global upper-mantle shear attenuation structure
815 by waveform tomography using the spectral element method’, *Geophysical Journal International*
816 **213**(3), 1536–1558.
- 817 Karato, S.-i. [1993], ‘Importance of anelasticity in the interpretation of seismic tomography’, *Geo-*
818 *physical research letters* **20**(15), 1623–1626.
- 819 Kido, M. and Čadež, O. [1997], ‘Inferences of viscosity from the oceanic geoid: Indication of a
820 low viscosity zone below the 660-km discontinuity’, *Earth and Planetary Science Letters* **151**(3-
821 4), 125–137.
- 822 Konishi, K., Fuji, N. and Deschamps, F. [2017], ‘Elastic and anelastic structure of the lowermost
823 mantle beneath the Western Pacific from waveform inversion’, *Geophysical Journal International*
824 **208**(3), 1290–1304.
- 825 Konishi, K., Fuji, N. and Deschamps, F. [2020], ‘Three-dimensional elastic and anelastic structure
826 of the lowermost mantle beneath the western Pacific from finite-frequency tomography’, *Journal*
827 *of Geophysical Research: Solid Earth* **125**(2), e2019JB018089.
- 828 Kovach, R. L. and Anderson, D. L. [1964], ‘Attenuation of shear waves in the upper and lower
829 mantle’, *Bulletin of the Seismological Society of America* **54**(6A), 1855–1864.
- 830 Lai, H., Garnero, E. J., Grand, S. P., Porritt, R. W. and Becker, T. W. [2019], ‘Global travel time
831 data set from adaptive empirical wavelet construction’, *Geochemistry, Geophysics, Geosystems*
832 **20**(5), 2175–2198.
- 833 Lau, H. C., Mitrovica, J. X., Auermann, J., Crawford, O., Al-Attar, D. and Letychev, K. [2016],
834 ‘Inferences of mantle viscosity based on ice age data sets: Radial structure’, *Journal of Geophys-*
835 *ical Research: Solid Earth* **121**(10), 6991–7012.
- 836 Lawrence, J. F. and Wyssession, M. E. [2006], ‘QLM9: A new radial quality factor ($Q\mu$) model for
837 the lower mantle’, *Earth and Planetary Science Letters* **241**(3-4), 962–971.

- 838 Lees, J. M. and Park, J. [1995], ‘Multiple-taper spectral analysis: A stand-alone C-subroutine’,
839 *Computers & Geosciences* **21**(2), 199–236.
- 840 Lekić, V., Matas, J., Panning, M. and Romanowicz, B. [2009], ‘Measurement and implications of
841 frequency dependence of attenuation’, *Earth and Planetary Science Letters* **282**(1-4), 285–293.
- 842 Liu, C. and Grand, S. P. [2018], ‘Seismic attenuation in the African LLSVP estimated from PcS
843 phases’, *Earth and Planetary Science Letters* **489**, 8–16.
- 844 Liu, H., Gurnis, M. and Leng, W. [2021], ‘Constraints on mantle viscosity from slab dynamics’,
845 *Journal of Geophysical Research: Solid Earth* **126**(8), e2021JB022329.
- 846 Mao, W. and Zhong, S. [2018], ‘Slab stagnation due to a reduced viscosity layer beneath the mantle
847 transition zone’, *Nature Geoscience* **11**(11), 876–881.
- 848 Mao, W. and Zhong, S. [2021], ‘Constraints on mantle viscosity from intermediate-wavelength
849 geoid anomalies in mantle convection models with plate motion history’, *Journal of Geophysical
850 Research: Solid Earth* **126**(4), e2020JB021561.
- 851 Marquardt, H. and Miyagi, L. [2015], ‘Slab stagnation in the shallow lower mantle linked to an
852 increase in mantle viscosity’, *Nature Geoscience* **8**(4), 311–314.
- 853 Masters, G., Woodhouse, J. and Freeman, G. [2011], ‘Mineos v1. 0.2 [software]’, *Computational
854 Infrastructure for Geodynamics* **99**.
- 855 Matas, J. and Bukowinski, M. S. [2007], ‘On the anelastic contribution to the temperature depen-
856 dence of lower mantle seismic velocities’, *Earth and Planetary Science Letters* **259**(1), 51–65.
857 **URL:** <https://www.sciencedirect.com/science/article/pii/S0012821X07002555>
- 858 Matheney, M. P. and Nowack, R. L. [1995], ‘Seismic attenuation values obtained from instantaneous-
859 frequency matching and spectral ratios’, *Geophysical Journal International* **123**(1), 1–15.
- 860 McCarthy, C., Takei, Y. and Hiraga, T. [2011], ‘Experimental study of attenuation and dispersion
861 over a broad frequency range: 2. The universal scaling of polycrystalline materials’, *Journal of
862 Geophysical Research: Solid Earth* **116**(B9).

863 Mitrovica, J. and Forte, A. [2004], ‘A new inference of mantle viscosity based upon joint inversion
864 of convection and glacial isostatic adjustment data’, *Earth and Planetary Science Letters* **225**(1-
865 2), 177–189.

866 Moulik, P. and Ekström, G. [2025], ‘Radial structure of the Earth: (II) Model features and inter-
867 pretations’, *Physics of the Earth and Planetary Interiors* **361**, 107320.
868 **URL:** <https://www.sciencedirect.com/science/article/pii/S0031920125000147>

869 Nguyen, V.-D., Nguyen, L.-M., Nguyen, C.-N., Ha, T.-G., Ha, V.-L., Nguyen, T.-H. and Le, Q.-
870 K. [2025], ‘Unveiling the seismic attenuation characteristics in the mantle beneath Southeast
871 Asia: Insights into mantle dynamics and tectonic processes’, *Regional Studies in Marine Science*
872 **86**, 104192.
873 **URL:** <https://www.sciencedirect.com/science/article/pii/S2352485525001835>

874 Ogiso, M. [2019], ‘A method for mapping intrinsic attenuation factors and scattering coefficients of S
875 waves in 3-D space and its application in southwestern Japan’, *Geophysical Journal International*
876 **216**(2), 948–957.

877 Okada, Y., Kasahara, K., Hori, S., Obara, K., Sekiguchi, S., Fujiwara, H. and Yamamoto, A. [2004],
878 ‘Recent progress of seismic observation networks in Japan—Hi-net, F-net, K-NET and KiK-net’,
879 **56**, xv–xxviii.

880 Oki, S. and Shearer, P. M. [2008], ‘Mantle Q structure from S-P differential attenuation measure-
881 ments’, *Journal of Geophysical Research: Solid Earth* **113**(B12).

882 Pang, G., Abers, G. A. and van Keken, P. E. [2023], ‘Focusing effects of teleseismic wavefields
883 by the subducting plate beneath Cascadia’, *Journal of Geophysical Research: Solid Earth*
884 **128**(6), e2022JB025486.

885 Pejić, T., Tkalčić, H., Sambridge, M., Cormier, V. F. and Benavente, R. [2017], ‘Attenuation
886 tomography of the upper inner core’, *Journal of Geophysical Research: Solid Earth* **122**(4), 3008–
887 3032.

888 Quan, Y. and Harris, J. M. [1997], ‘Seismic attenuation tomography using the frequency shift
889 method’, *Geophysics* **62**(3), 895–905.

- 890 Reid, F., Woodhouse, J. and Van Heijst, H. [2001], ‘Upper mantle attenuation and velocity structure
891 from measurements of differential S phases’, *Geophysical Journal International* **145**(3), 615–630.
- 892 Resovsky, J., Trampert, J. and Van der Hilst, R. [2005], ‘Error bars for the global seismic Q profile’,
893 *Earth and Planetary Science Letters* **230**(3), 413–423.
- 894 **URL:** <https://www.sciencedirect.com/science/article/pii/S0012821X04007137>
- 895 Revenaugh, J. and Jordan, T. H. [1991], ‘Mantle Layering From ScS Reverberations: 1. Waveform
896 Inversion From Zeroth-Order Reverberations’, *Journal of Geophysical Research: Solid Earth*
897 **96**(B12), 19749–19762.
- 898 Ricard, Y., Durand, S., Montagner, J.-P. and Chambat, F. [2014], ‘Is there seismic attenuation in
899 the mantle?’, *Earth and Planetary Science Letters* **388**, 257–264.
- 900 Ricard, Y. and Wuming, B. [1991], ‘Inferring the viscosity and the 3-D density structure of the man-
901 tle from geoid, topography and plate velocities’, *Geophysical Journal International* **105**(3), 561–
902 571.
- 903 Rietbrock, A. [2001], ‘P wave attenuation structure in the fault area of the 1995 Kobe earthquake’,
904 *Journal of Geophysical Research: Solid Earth* **106**(B3), 4141–4154.
- 905 **URL:** <https://agupubs.onlinelibrary.wiley.com/doi/abs/10.1029/2000JB900234>
- 906 Ritsema, J., Deuss, A., Van Heijst, H. and Woodhouse, J. [2011], ‘S40RTS: a degree-40 shear-
907 velocity model for the mantle from new Rayleigh wave dispersion, teleseismic traveltime and
908 normal-mode splitting function measurements’, *Geophysical Journal International* **184**(3), 1223–
909 1236.
- 910 Romanowicz, B. [1995], ‘A global tomographic model of shear attenuation in the upper mantle’,
911 *Journal of Geophysical Research: Solid Earth* **100**(B7), 12375–12394.
- 912 Romanowicz, B. [1998], ‘Attenuation tomography of the Earth’s mantle: a review of current status’,
913 *pure and applied geophysics* **153**, 257–272.
- 914 Romanowicz, B. and Gung, Y. [2002], ‘Superplumes from the core-mantle boundary to the litho-
915 sphere: Implications for heat flux’, *Science* **296**(5567), 513–516.

- 916 Romanowicz, B. and Mitchell, B. [2015], ‘1.25—Deep Earth Structure: Q of the Earth from crust
917 to core’, *Treatise on geophysics* **1**, 789–827.
- 918 Rost, S., Earle, P. S., Shearer, P. M., Frost, D. A. and Selby, N. D. [2015], Seismic detections of
919 small-scale heterogeneities in the deep Earth, *in* ‘The Earth’s heterogeneous mantle: A geophys-
920 ical, geodynamical, and geochemical perspective’, Springer, pp. 367–390.
- 921 Rost, S. and Frost, D. A. [2025], ‘Global mantle heterogeneity structure from scattered PKPPKP’,
922 *Earth and Planetary Science Letters* **664**, 119415.
923 **URL:** <https://www.sciencedirect.com/science/article/pii/S0012821X25002146>
- 924 Roth, E. G., Wiens, D. A., Dorman, L. M., Hildebrand, J. and Webb, S. C. [1999], ‘Seismic atten-
925 uation tomography of the Tonga-Fiji region using phase pair methods’, *Journal of Geophysical*
926 *Research: Solid Earth* **104**(B3), 4795–4809.
927 **URL:** <https://agupubs.onlinelibrary.wiley.com/doi/abs/10.1029/1998JB900052>
- 928 Rudolph, M. L., Lekić, V. and Lithgow-Bertelloni, C. [2015], ‘Viscosity jump in Earth’s mid-
929 mantle’, *Science* **350**(6266), 1349–1352.
930 **URL:** <https://www.science.org/doi/abs/10.1126/science.aad1929>
- 931 Rudolph, M., Moulik, P. and Lekić, V. [2020], ‘Bayesian inference of mantle viscosity from whole-
932 mantle density models’, *Geochemistry, Geophysics, Geosystems* **21**(11), e2020GC009335.
- 933 Scherbaum, F. [1990], ‘Combined inversion for the three-dimensional Q structure and source
934 parameters using microearthquake spectra’, *Journal of Geophysical Research: Solid Earth*
935 **95**(B8), 12423–12438.
936 **URL:** <https://agupubs.onlinelibrary.wiley.com/doi/abs/10.1029/JB095iB08p12423>
- 937 Schultz, R. and Gu, Y. J. [2013], ‘Multiresolution imaging of mantle reflectivity structure using SS
938 and PP precursors’, *Geophysical Journal International* **195**(1), 668–683.
939 **URL:** <https://doi.org/10.1093/gji/ggt266>
- 940 Shearer, P. [2007], 1.20 - Deep Earth Structure – Seismic Scattering in the Deep Earth, *in* G. Schu-
941 bert, ed., ‘Treatise on Geophysics’, Elsevier, Amsterdam, pp. 695–729.
942 **URL:** <https://www.sciencedirect.com/science/article/pii/B9780444527486000213>

- 943 Shearer, P. M. [1993], ‘Global mapping of upper mantle reflectors from long-period SS precursors’,
944 *Geophysical Journal International* **115**(3), 878–904.
- 945 Sheehan, A. F. and Solomon, S. C. [1992], ‘Differential shear wave attenuation and its lateral varia-
946 tion in the North Atlantic region’, *Journal of Geophysical Research: Solid Earth* **97**(B11), 15339–
947 15350.
- 948 Soto Castaneda, R. A., Abers, G. A., Eilon, Z. C. and Christensen, D. H. [2021], ‘Teleseismic At-
949 tenuation, Temperature, and Melt of the Upper Mantle in the Alaska Subduction Zone’, *Journal*
950 *of Geophysical Research: Solid Earth* **126**(7), e2021JB021653.
951 **URL:** <https://agupubs.onlinelibrary.wiley.com/doi/abs/10.1029/2021JB021653>
- 952 Souriau, A., Rivera, L., Maggi, A. and L ev eque, J.-J. [2012], ‘Seismic attenuation in the eastern
953 Australian and Antarctic plates, from multiple ScS waves’, *Geophysical Journal International*
954 **190**(1), 569–579.
955 **URL:** <https://doi.org/10.1111/j.1365-246X.2012.05501.x>
- 956 Steinberger, B., Werner, S. C. and Torsvik, T. H. [2010], ‘Deep versus shallow origin of gravity
957 anomalies, topography and volcanism on Earth, Venus and Mars’, *Icarus* **207**(2), 564–577.
958 **URL:** <https://www.sciencedirect.com/science/article/pii/S0019103509005168>
- 959 Suetsugu, D., Shiobara, H., Sugioka, H., Ito, A., Isse, T., Ishihara, Y., Tanaka, S., Obayashi, M.,
960 Tonegawa, T., Yoshimitsu, J. and Kobayashi, T. [2019], ‘High Q ScS beneath the Ontong Java
961 Plateau’, *Earth, Planets and Space* **71**, 1–9.
- 962 Sun, S., Ricard, Y., Durand, S. and Debayle, E. [2025], ‘A high attenuation layer around 1000 km
963 depth’, *Earth and Planetary Science Letters* **669**, 119577.
- 964 Talavera-Soza, S., Cobden, L., Faul, U. H. and Deuss, A. [2025], ‘Global 3D model of mantle
965 attenuation using seismic normal modes’, *Nature* **637**(8048), 1131–1135.
- 966 Tanaka, S. and Tkal ci c, H. [2015], ‘Complex inner core boundary from frequency characteristics of
967 the reflection coefficients of PKiKP waves observed by Hi-net’, *Progress in Earth and Planetary*
968 *Science* **2**(1), 34.

- 969 Teng, T.-L. [1968], ‘Attenuation of body waves and the Q structure of the mantle’, *Journal of*
970 *Geophysical Research* **73**(6), 2195–2208.
- 971 Thomson, D. [1982], ‘Spectrum estimation and harmonic analysis’, *Proceedings of the IEEE*
972 **70**(9), 1055–1096.
- 973 Thrastarson, S., van Herwaarden, D.-P., Noe, S., Josef Schiller, C. and Fichtner, A. [2024], ‘RE-
974 VEAL: A global full-waveform inversion model’, **114**(3), 1392–1406.
- 975 Tian, D. [2024], ‘HinetPy: A Python package for accessing and processing NIED Hi-net seismic
976 data’, **9**(98), 6840.
- 977 Wang, X., Li, Q., Li, G., Zhou, Y., Ye, Z. and Zhang, H. [2018], ‘Seismic triplication used to reveal
978 slab subduction that had disappeared in the late Mesozoic beneath the northeastern South China
979 Sea’, *Tectonophysics* **727**, 28–40.
- 980 Warren, L. M. and Shearer, P. M. [2002], ‘Mapping lateral variations in upper mantle attenuation
981 by stacking P and PP spectra’, *Journal of Geophysical Research: Solid Earth* **107**(B12), ESE
982 6–1–ESE 6–11.
983 **URL:** <https://agupubs.onlinelibrary.wiley.com/doi/abs/10.1029/2001JB001195>
- 984 Warren, L. M. and Shearer, P. M. [2006], ‘Systematic determination of earthquake rupture di-
985 rectivity and fault planes from analysis of long-period P-wave spectra’, *Geophysical Journal*
986 *International* **164**(1), 46–62.
- 987 Waszek, L. and Deuss, A. [2013], ‘A low attenuation layer in the Earth’s uppermost inner core’,
988 *Geophysical Journal International* **195**(3), 2005–2015.
989 **URL:** <https://doi.org/10.1093/gji/ggt368>
- 990 Waszek, L., Schmerr, N. C. and Ballmer, M. D. [2018], ‘Global observations of reflectors in the mid-
991 mantle with implications for mantle structure and dynamics’, *Nature communications* **9**(1), 385.
- 992 Weber, Z. [2000], ‘Seismic traveltime tomography: a simulated annealing approach’, *Physics of the*
993 *Earth and Planetary Interiors* **119**(1-2), 149–159.

- 994 Widmer, R., Masters, G. and Gilbert, F. [1991], ‘Spherically symmetric attenuation within the
995 Earth from normal mode data’, *Geophysical journal international* **104**(3), 541–553.
- 996 Woodhouse, J. [1988], ‘The calculation of the eigenfrequencies and eigenfunctions of the free oscil-
997 lations of the Earth and Sun’, *Seismological algorithms: computational methods and computer*
998 *programs* pp. 321–370.
- 999 Zaroli, C., Debayle, E. and Sambridge, M. [2010], ‘Frequency-dependent effects on global S-wave
1000 traveltimes: wavefront-healing, scattering and attenuation’, *Geophysical Journal International*
1001 **182**(2), 1025–1042.
- 1002 Zhang, B., Ni, S. and Chen, Y. [2019], ‘Seismic attenuation in the lower mantle beneath Northeast
1003 China constrained from short-period reflected core phases at short epicentral distances’, *Earth*
1004 *and Planetary Physics* **3**(6), 537–546.
- 1005 Zhao, C., Garnero, E. J., McNamara, A. K., Schmerr, N. and Carlson, R. W. [2015], ‘Seismic evi-
1006 dence for a chemically distinct thermochemical reservoir in Earth’s deep mantle beneath Hawaii’,
1007 *Earth and Planetary Science Letters* **426**, 143–153.
- 1008 Zhu, M., Sun, S., Zhou, Y. and Wu, Q. [2022], ‘Mantle Q structure from S, SS, SSS and SSSS
1009 amplitude measurements’, *Geophysical Journal International* **231**(1), 703–716.

1 Supplementary materials for

2 Q_{M1D} : A 1D model of shear attenuation in the mantle from
3 differential body waves

4 Carl Martin^{1,2*}, Sujania Talavera-Soza¹ & Arwen Deuss¹

5 ¹ Department of Geosciences, Utrecht University, 3584 CB, Netherlands

6 ² Research School of Earth Sciences, The Australian National University, Canberra, ACT
7 0200, Australia

8 *Corresponding author (carl.martin@anu.edu.au)

9 **SUPPLEMENTARY**

10 In this supplementary are:

- 11 • Figures S1–S12

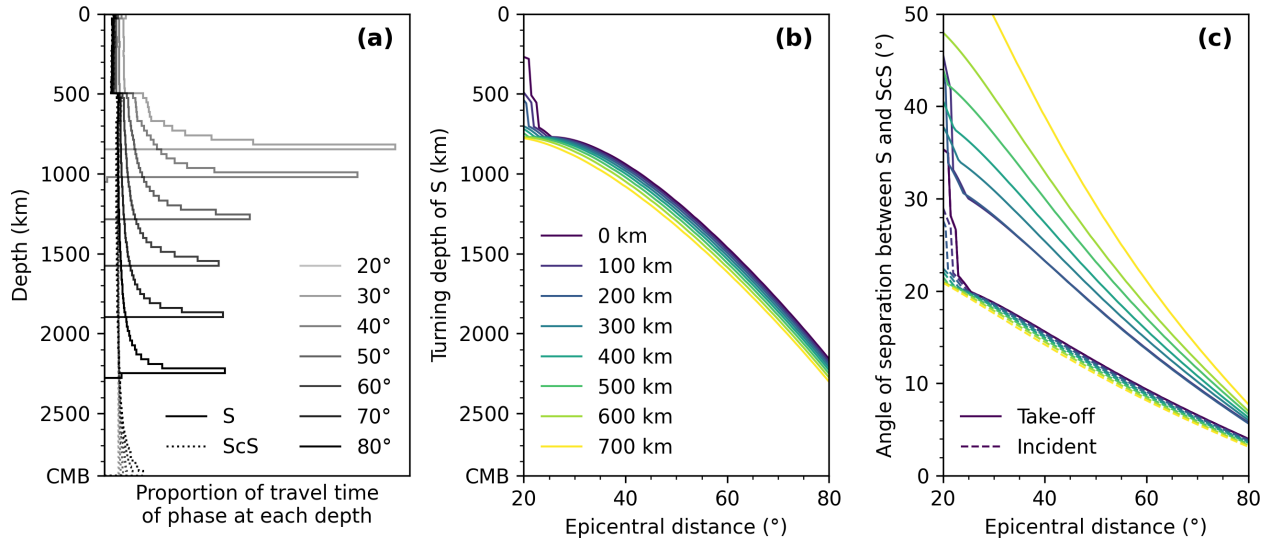


Figure S1: (a) The proportion of travel time of each of S and ScS body waves spent at each depth as a function of epicentral distance. (b) The turning depth of S waves as a function of epicentral distance. (c) The difference in angle between S and ScS raypaths at take-off (from the event) and incident (at the receiver).

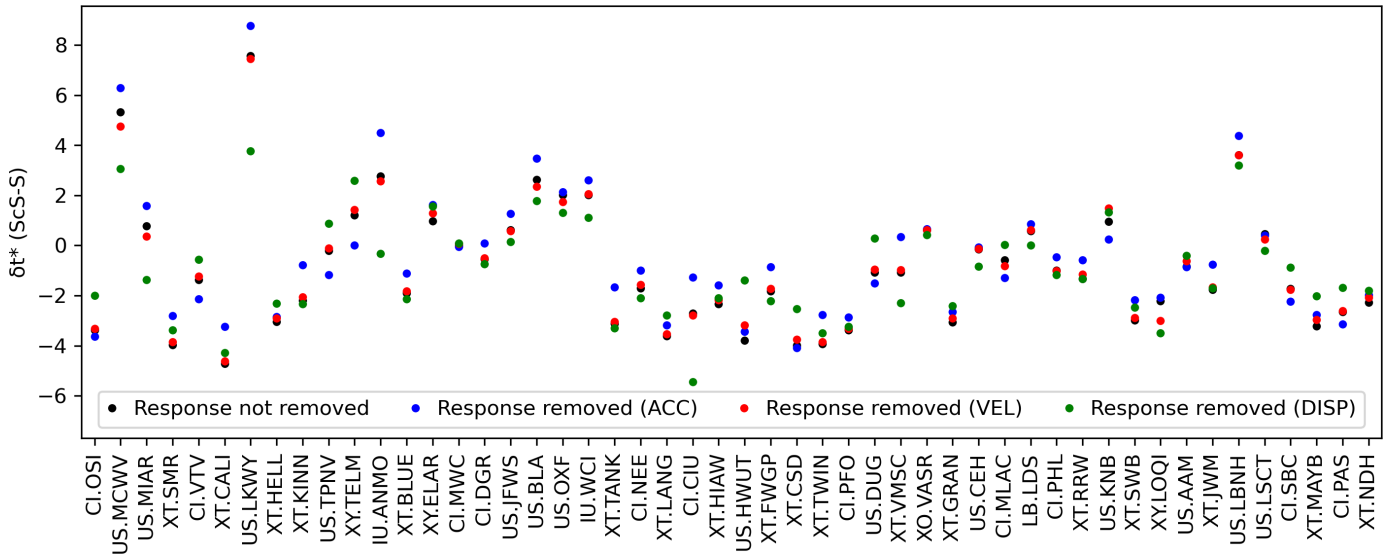


Figure S2: $\delta t^*_{\text{ScS-S}}$ measurements for a selection of 50 stations for the event on 1997/11/28, as used by Ford et al. [2012], for data which has been downloaded. Values are for data with station response not removed (black) and removed and processed as acceleration (blue), velocity (red), and displacement (green).

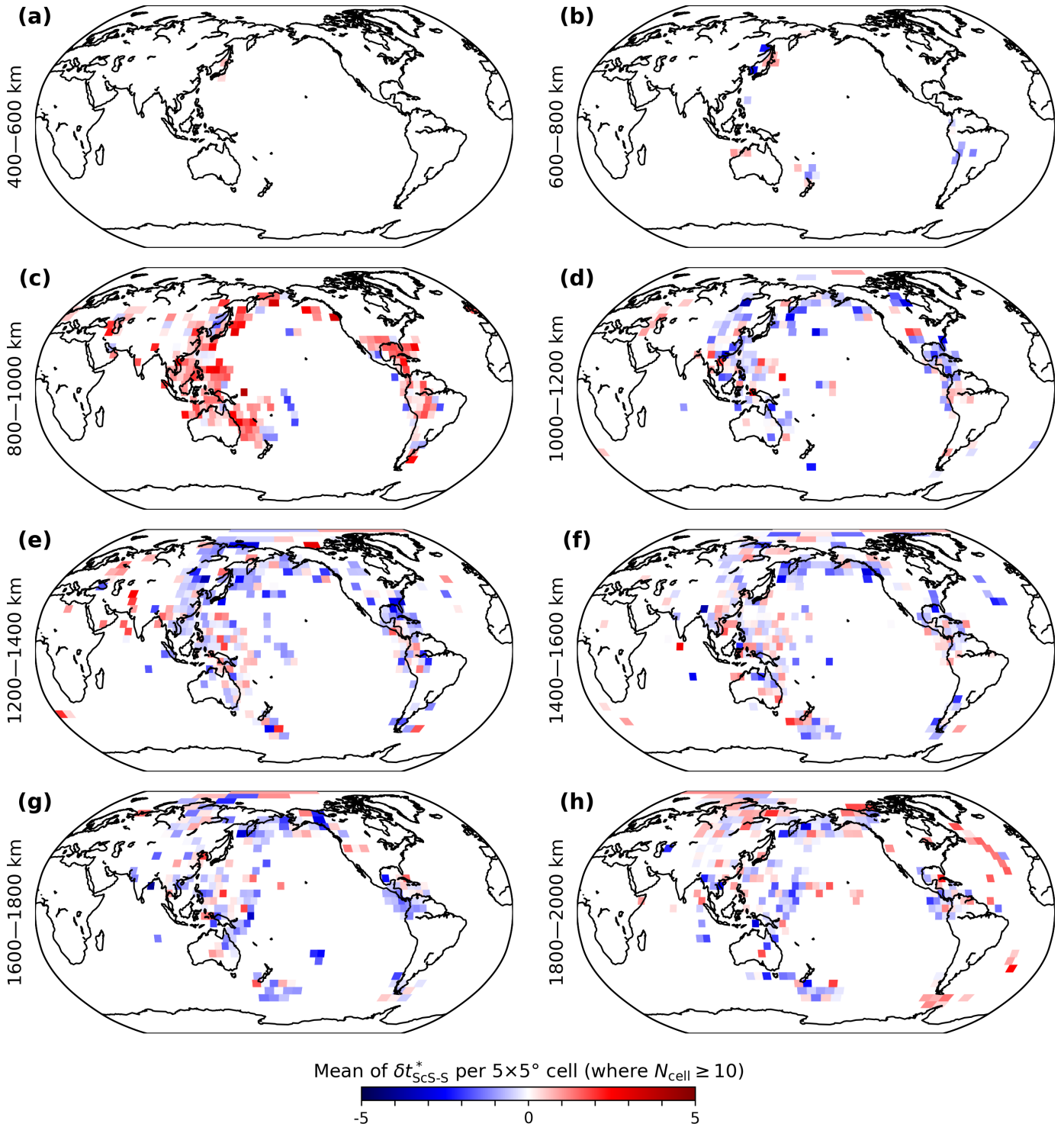


Figure S3: Mean value of $\delta t_{\text{ScS-S}}^*$ per $5 \times 5^\circ$ quasi-equal area cell where grid cells with fewer than 10 ScS bounce points have been omitted, binned according to the turning depth of the S raypath: (a) 400–600, (b) 600–800, (c) 800–1000, (d) 1000–1200, (e) 1200–1400, (f) 1400–1600, (g) 1600–1800 and (h) 1800–2000 km.

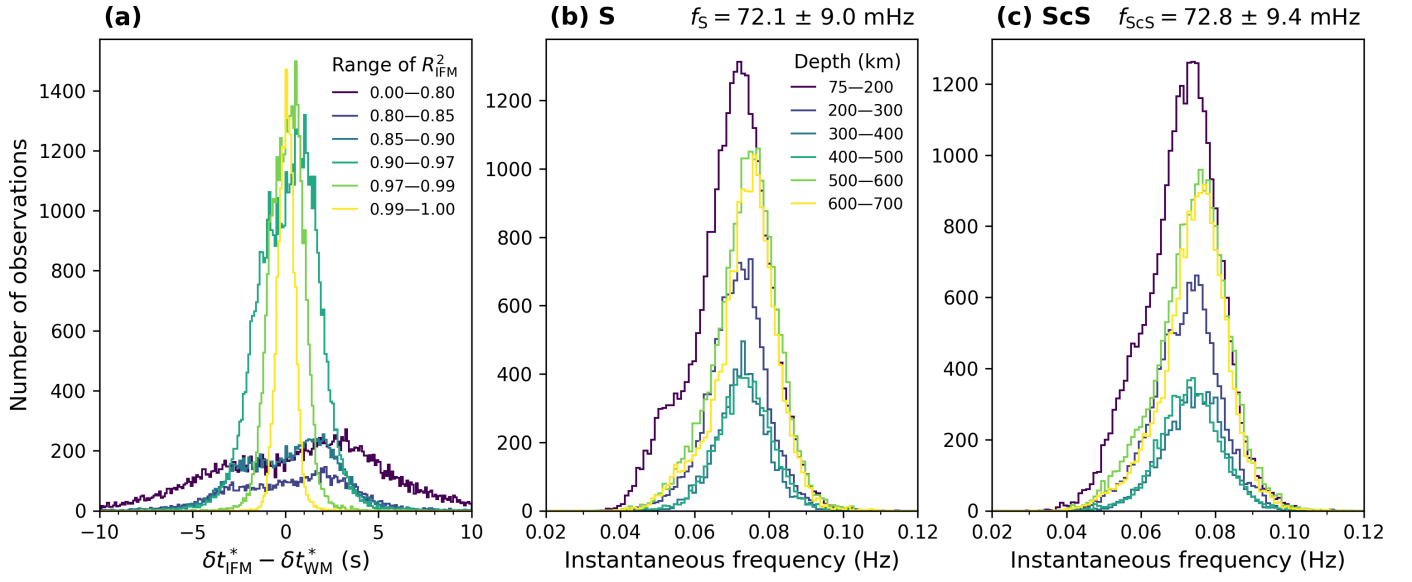


Figure S4: Histograms of (a) the difference between measurements of relative attenuation from the instantaneous frequency matching (IFM) and waveform matching (WM) methods, and instantaneous frequency measurements of (b) S and (c) ScS, binned by event depth. On average, $f_S < f_{\text{ScS}}$, indicating that S is more attenuated than ScS.

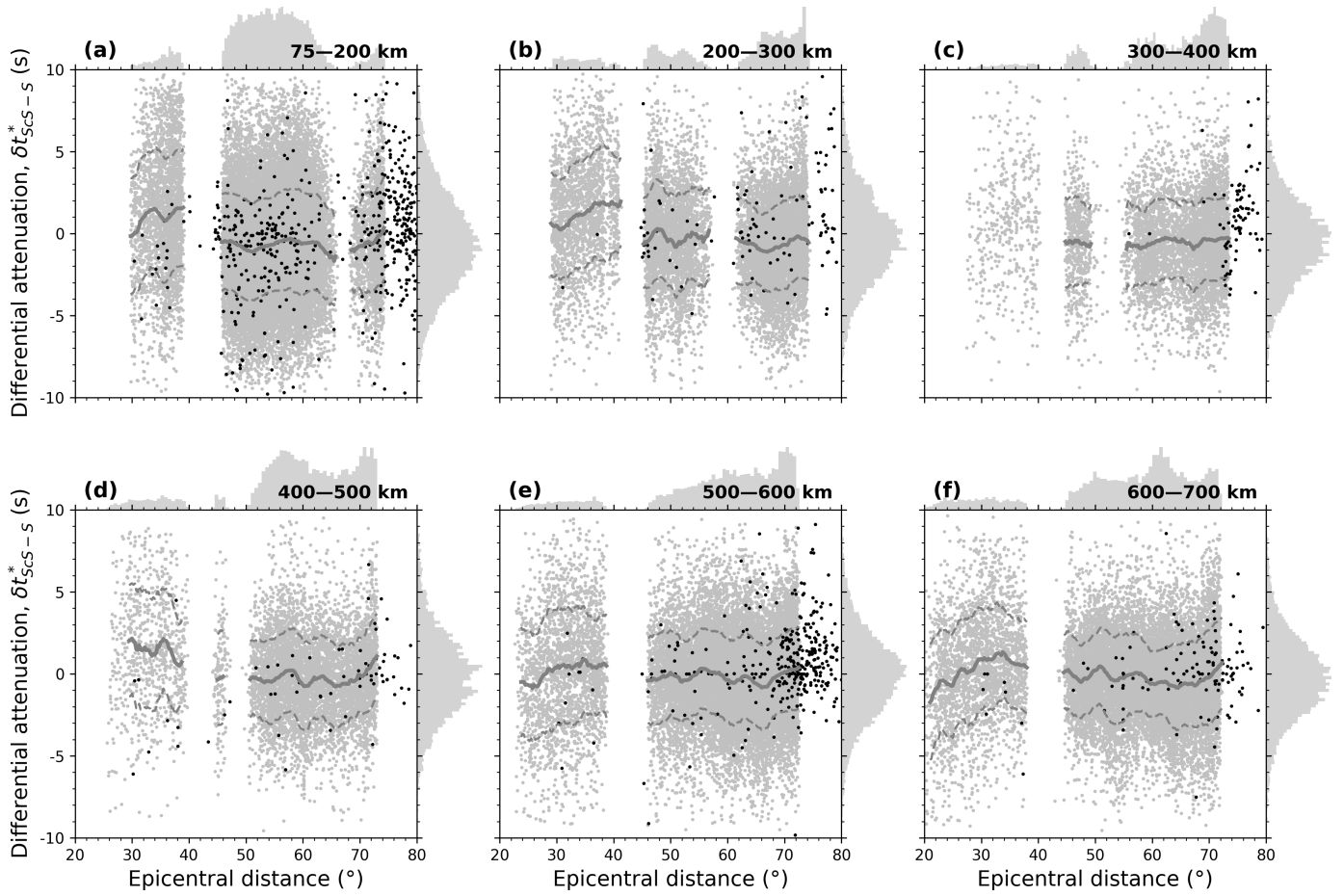


Figure S5: The dataset of differential attenuation $\delta t_{\text{ScS}-s}^*$ measurements reproduced from Figure 5 (grey dots), with constructed measurements of differential attenuation $t_{\text{ScS}}^* - t_{\text{S}}^*$ from the published dataset of Lai et al. [2019] (black dots). Aggregated trends of these measurements for events deeper and shallower than 200 km are plotted in Figure 7 in the main paper (solid and dashed blue lines, respectively).

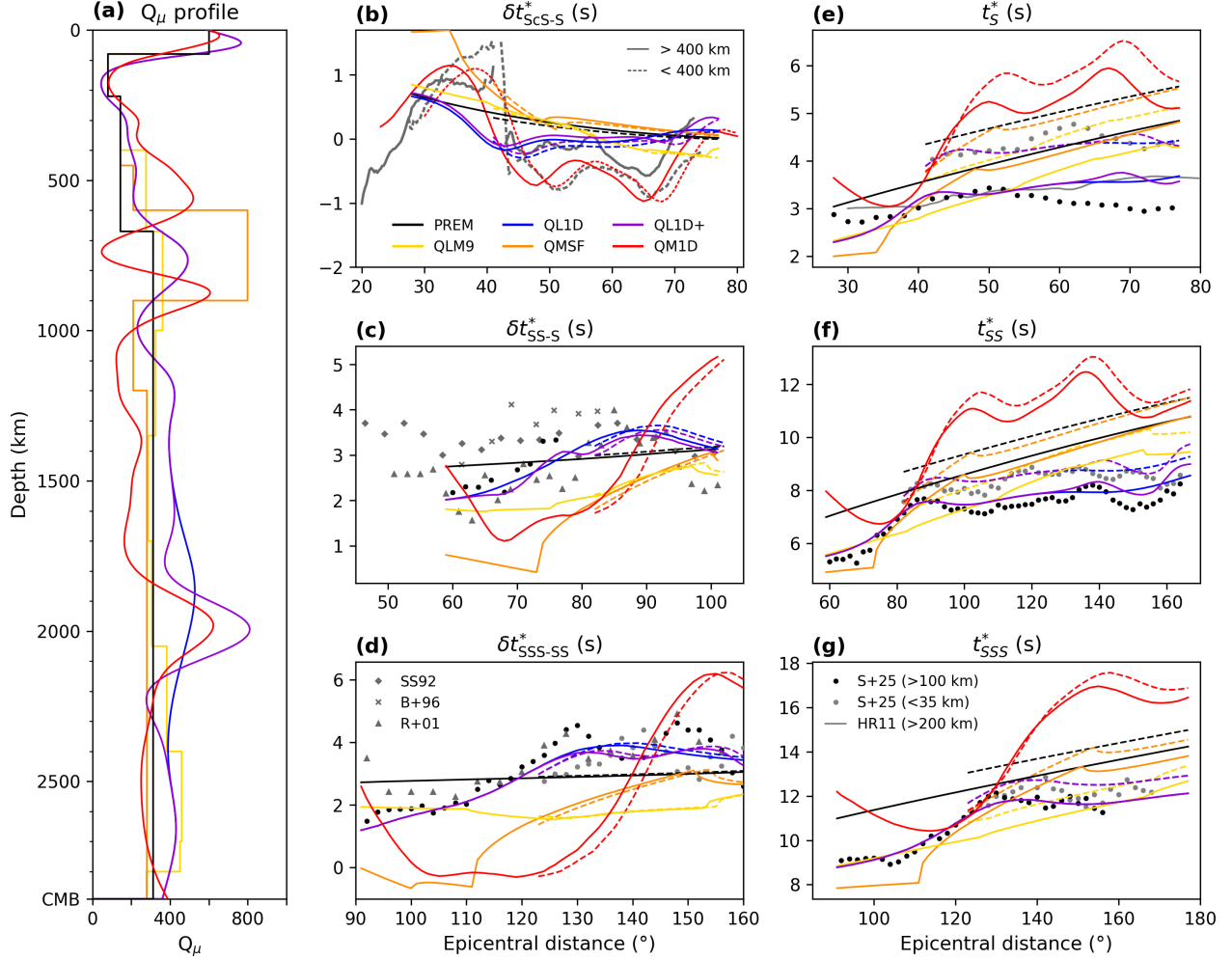


Figure S6: **(a)** Q_μ profiles of PREM (black), QLM9 (yellow), QMSF (orange), Q_{MID} (red), Q_{LID} (blue) and a modified version of Q_{LID} with a Ricker wavelet superimposed at a depth of 2000 km (purple). **(b)** Predictions of relative attenuation δt_{SCS-S}^* for each of the models overlaid on data from this study, using a 5° rolling window, for deeper (> 400 km, solid) and shallower (> 400 km, dashed) events. Predictions of differential attenuation **(c)** δt_{SS-S}^* and **(d)** δt_{SSS-SS}^* and absolute attenuation **(e)** t_S^* , **(f)** t_{SS}^* and **(g)** t_{SSS}^* for each of the Q_μ profiles. The mean measurements of δt_{SS-S}^* , δt_{SSS-SS}^* , t_S^* , t_{SS}^* and t_{SSS}^* for deep (black dots) and shallow (grey dots) events were constructed from the Sun et al. [2025] dataset. Datasets from other studies are also included for reference where aggregated data was available: t_S^* by Hwang and Ritsema [2011] (grey line, note that data has been fixed to match PREM at 30°); δt_{SS-S}^* by Sheehan and Solomon [1992] (grey crosses) and Bhattacharyya et al. [1996] (grey diamonds); and δt_{SS-S}^* and δt_{SSS-SS}^* by Reid et al. [2001] (grey triangles).

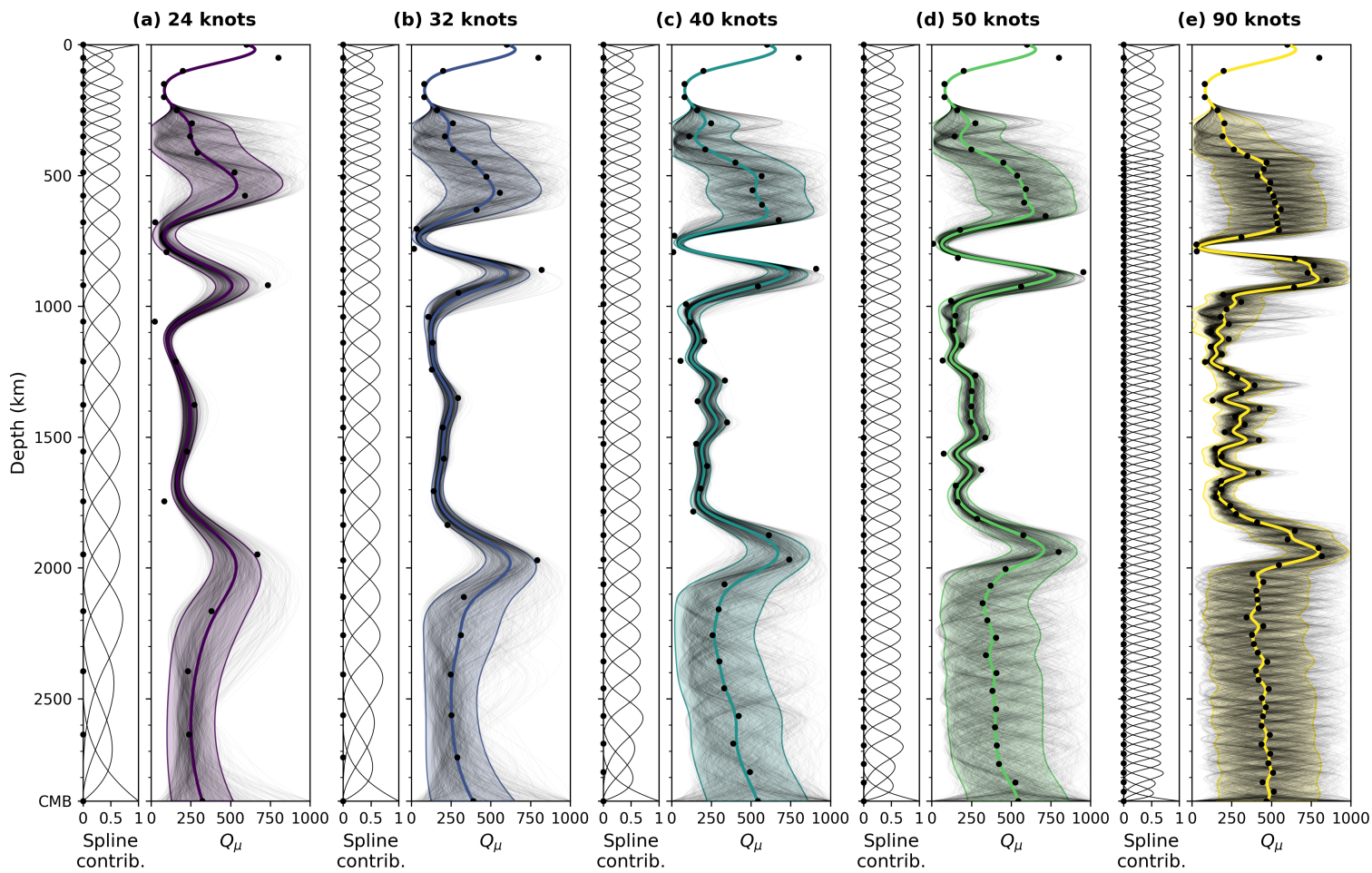


Figure S7: Cubic B-spline basis functions and inversion results for (a) 24, (b) 32, (c) 40, (d) 50 and (e) 90 depth knots.

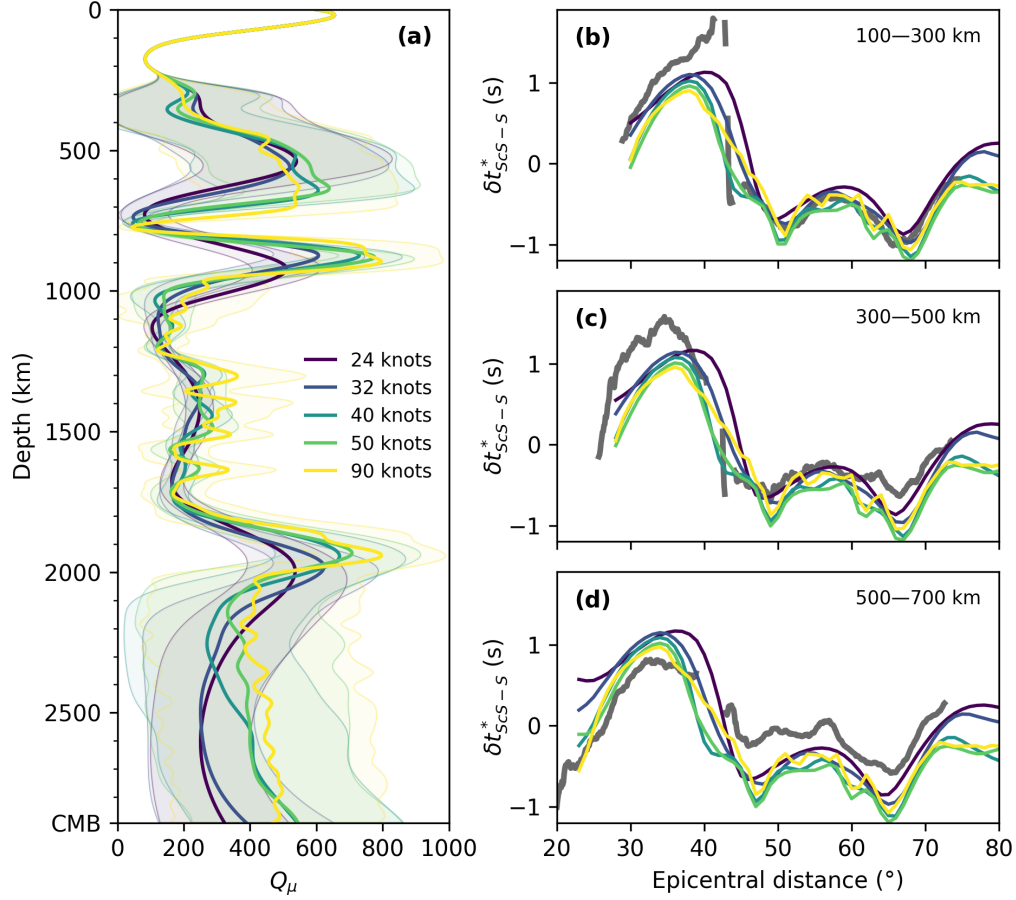


Figure S8: (a) Comparison of mean inversion Q_μ profiles for the different numbers of depth knots in Figure S7. Predictions of $\delta t_{\text{SCS-S}}^*$ for each of the models overlaid on data from this study for event depths (b) 100–300, (c) 300–500 and (d) 500–700 km, using a 5° rolling window.

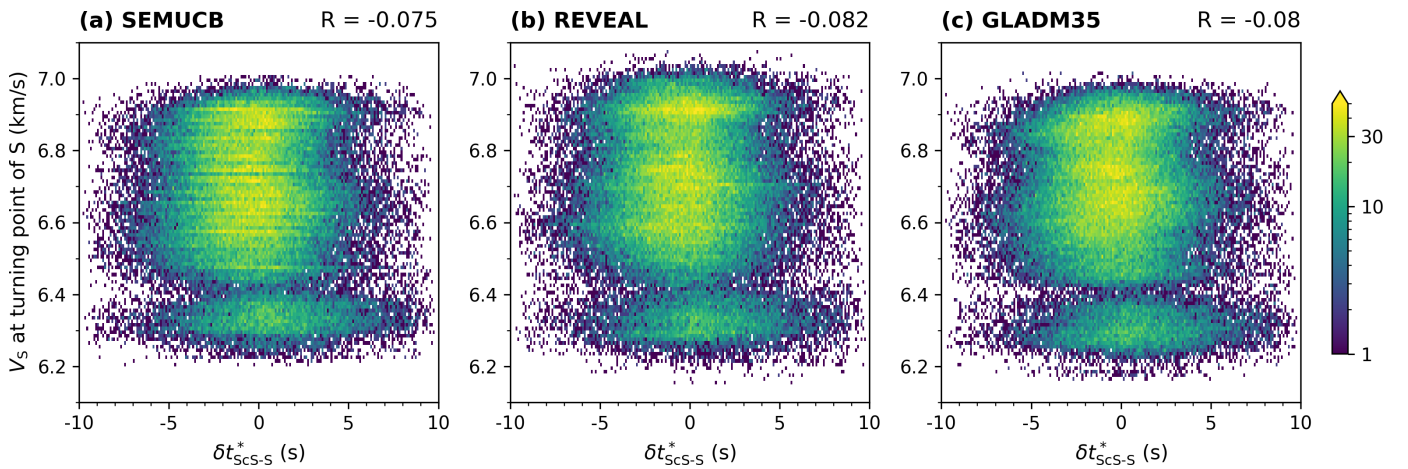


Figure S9: Plots of our measured values of $\delta t_{\text{SCS-S}}^*$ compared to the velocity at the turning depth of the S raypaths for three full waveform tomographic models of the mantle: (a) SEMUCB-WM1 [French and Romanowicz, 2014], (b) REVEAL [Thrustarson et al., 2024] and (c) GLAD-M35 [Cui et al., 2024]. The Pearson correlation coefficient R is computed for each comparison.

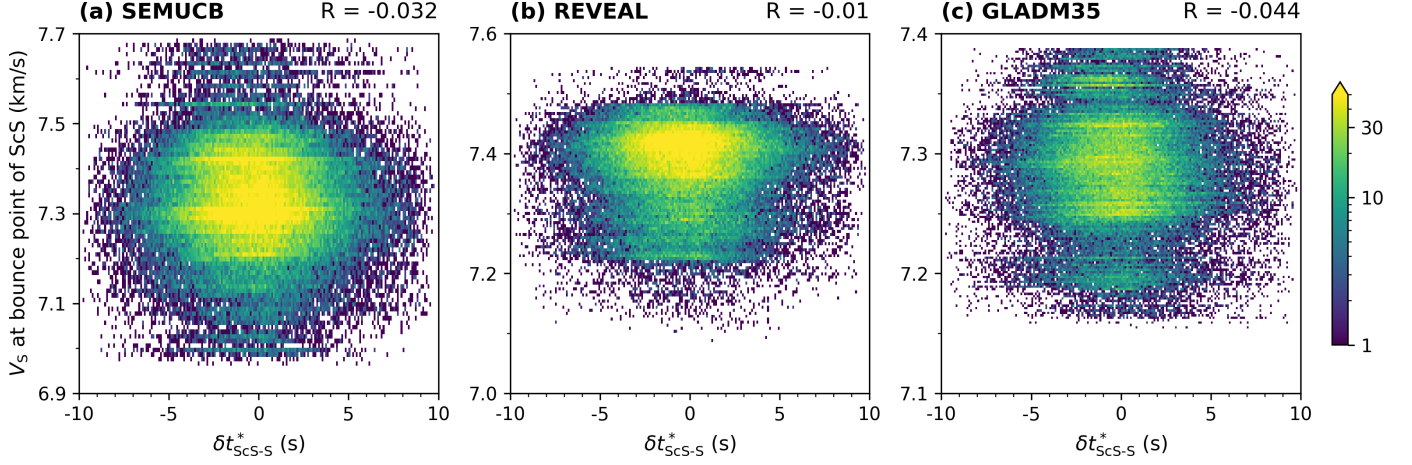


Figure S10: Plots of our measured values of $\delta t_{\text{ScS-S}}^*$ compared to the velocity at the bounce point of the ScS raypaths for three full waveform tomographic models of the mantle: **(a)** SEMUCB-WM1 [French and Romanowicz, 2014], **(b)** REVEAL [Thrustarson et al., 2024] and **(c)** GLAD-M35 [Cui et al., 2024]. The Pearson correlation coefficient R is computed for each comparison.

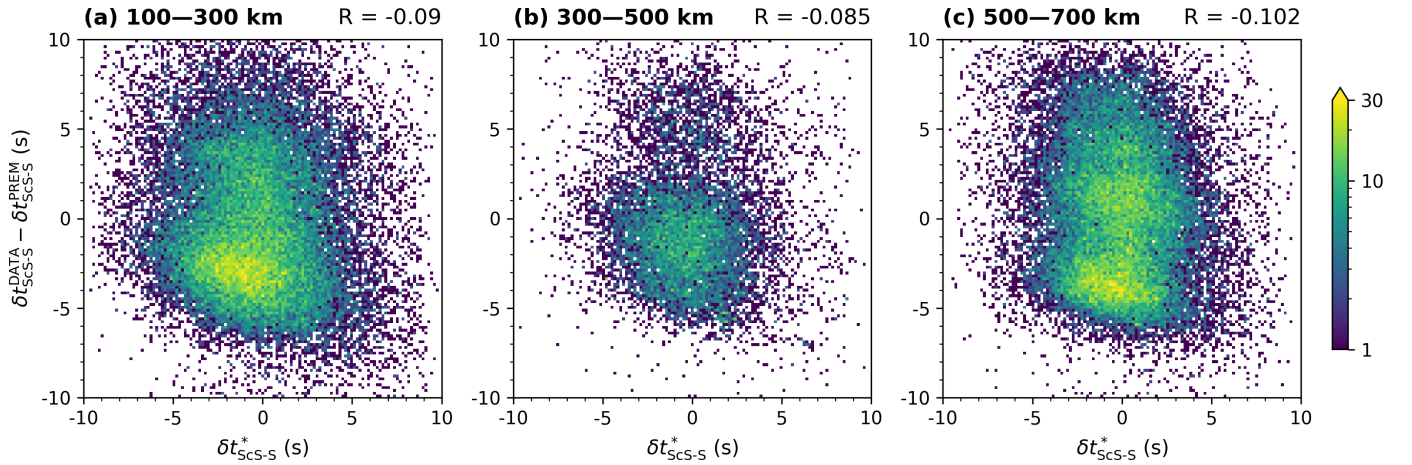


Figure S11: Plots of our measured values of $\delta t_{\text{ScS-S}}^*$ compared to the difference between the observed travel time differences (corrected for attenuation) and predicted travel time differences for PREM $\delta t_{\text{ScS-S}}^{\text{DATA}} - \delta t_{\text{ScS-S}}^{\text{PREM}}$, for the same event depth ranges as Figure S8: **(a)** 100–300, **(b)** 300–500 and **(c)** 500–700 km. The Pearson correlation coefficient R is computed for each comparison.

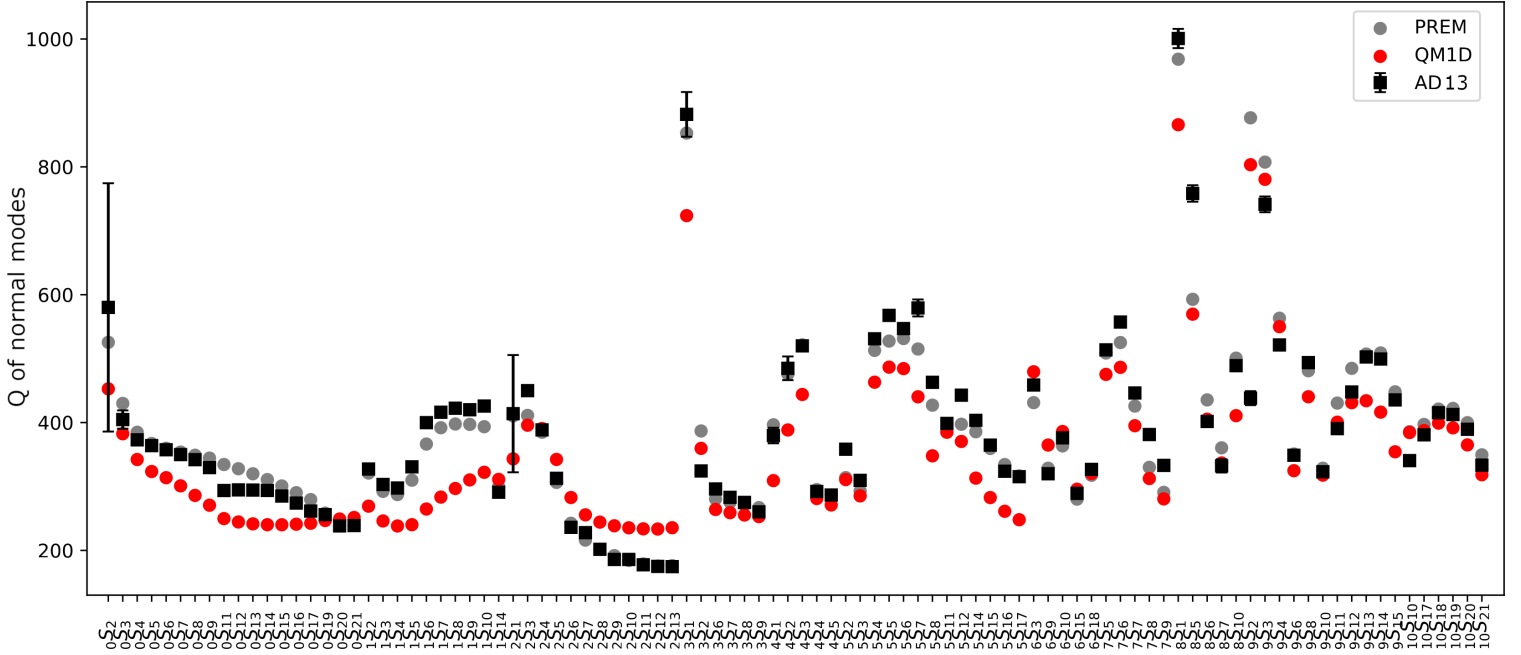


Figure S12: Values of quality factor Q of normal modes for both PREM (grey) and our model Q_{M1D} (red) computed using MINEOS [Woodhouse, 1988; Masters et al., 2011], with all other parameters kept the same as PREM and assuming that $\alpha = 0$. Measured values of Q of normal modes from Deuss et al. [2013] (black) are overlaid.

References

- Bhattacharyya, J., Masters, G. and Shearer, P. [1996], ‘Global lateral variations of shear wave attenuation in the upper mantle’, *Journal of Geophysical Research: Solid Earth* **101**(B10), 22273–22289.
- Cui, C., Lei, W., Liu, Q., Peter, D., Bozdağ, E., Tromp, J., Hill, J., Podhorszki, N. and Pugmire, D. [2024], ‘GLAD-M35: a joint P and S global tomographic model with uncertainty quantification’, *Geophysical Journal International* **239**(1), 478–502.
- Deuss, A., Ritsema, J. and van Heijst, H. [2013], ‘A new catalogue of normal-mode splitting function measurements up to 10 mHz’, *Geophysical Journal International* **193**(2), 920–937.
- Ford, S. R., Garnero, E. J. and Thorne, M. S. [2012], ‘Differential t^* measurements via instantaneous frequency matching: observations of lower mantle shear attenuation heterogeneity beneath western central america’, *Geophysical Journal International* **189**(1), 513–523.
- French, S. and Romanowicz, B. A. [2014], ‘Whole-mantle radially anisotropic shear velocity structure from spectral-element waveform tomography’, **199**(3), 1303–1327.
- Hwang, Y. K. and Ritsema, J. [2011], ‘Radial $Q\mu$ structure of the lower mantle from teleseismic body-wave spectra’, *Earth and Planetary Science Letters* **303**(3-4), 369–375.
- Lai, H., Garnero, E. J., Grand, S. P., Porritt, R. W. and Becker, T. W. [2019], ‘Global travel time data set from adaptive empirical wavelet construction’, *Geochemistry, Geophysics, Geosystems* **20**(5), 2175–2198.
- Masters, G., Woodhouse, J. and Freeman, G. [2011], ‘Mineos v1. 0.2 [software]’, *Computational Infrastructure for Geodynamics* **99**.
- Reid, F., Woodhouse, J. and Van Heijst, H. [2001], ‘Upper mantle attenuation and velocity structure from measurements of differential S phases’, *Geophysical Journal International* **145**(3), 615–630.
- Sheehan, A. F. and Solomon, S. C. [1992], ‘Differential shear wave attenuation and its lateral variation in the North Atlantic region’, *Journal of Geophysical Research: Solid Earth* **97**(B11), 15339–15350.

- 38 Sun, S., Ricard, Y., Durand, S. and Debayle, E. [2025], ‘A high attenuation layer around 1000 km
39 depth’, *Earth and Planetary Science Letters* **669**, 119577.
- 40 Thrastarson, S., van Herwaarden, D.-P., Noe, S., Josef Schiller, C. and Fichtner, A. [2024], ‘RE-
41 VEAL: A global full-waveform inversion model’, **114**(3), 1392–1406.
- 42 Woodhouse, J. [1988], ‘The calculation of the eigenfrequencies and eigenfunctions of the free oscil-
43 lations of the Earth and Sun’, *Seismological algorithms: computational methods and computer*
44 *programs* pp. 321–370.